Effects of swell waves caused by atmospheric depression on ships sailing in the North Pacific ocean

Lee, Sang-Won

Sasa, Kenji

Masagaki, Tomoya

Chen, Chen

(Citation)
Ocean Engineering,312:119121

(Issue Date)
2024-11-15

(Resource Type)
journal article

(Version)
Version of Record

Ocean Engineering 312 (2024) 119121

Contents lists available at ScienceDirect

Ocean Engineering

journal homepage: www.elsevier.com/locate/oceaneng

ELSEVIER

Research paper

Effects of swell waves caused by atmospheric depression on ships sailing in the North Pacific ocean

Sang-Won Lee [a], Kenji Sasa [a,*], Tomoya Masagaki [a], Chen Chen [b]

[a] Graduate School of Maritime Sciences, Kobe University, Japan
[b] School of Navigation, Wuhan University of Technology, Wuhan, China

ARTICLE INFO

Keywords:
Swell wave
Long-period wave
Ship motion
Regression model
Wave simulation
Onboard measurement

ABSTRACT

The surge in maritime traffic has spurred the construction of large vessels, including very large ore carriers and mega containerships. These immense vessels are susceptible to accident risks owing to the considerable ship motions induced by long-period waves. Despite this, long-period waves such as swell waves have not been leveraged for navigation purposes, owing to the facts that avoidance of atmospheric depression has been main concern. This study endeavors to address this gap by employing several regression models to predict swell wave height using significant wave height and mean wave period. Furthermore, a range of wave simulation scenarios is utilized to replicate swell waves and confirm the wave conditions stemming from distinct atmospheric depressions. Ship motion estimations are derived under these wave conditions and compared with onboard measurement data. The regression model incorporating $\sqrt{H_{1/3}} \times T_{mean}$ showed the highest accuracy in estimating swell waves. Additionally, ship motion estimations solely considering the swell wave components demonstrated practical accuracy in comparison with ship motions influenced by all wave components. This study is constrained by its focus on a limited timeframe and region within the North Pacific. Nevertheless, its findings hold promise for enhancing ship and port operations when applied to various periods and regions.

1. Introduction

Despite enduring global crises such as COVID-19 and the war in Ukraine, maritime transportation remains the cornerstone of global trade, constituting over 90 percent of the total cargo volume. Furthermore, according to the United Nations Conference on Trade and Development (UNCTAD), maritime trade is projected to expand by 2.4 percent in 2023 and by an additional 2.1 percent from 2024 to 2028 (UNCTAD, 2023). As the demand for maritime transportation continues to increase, there has been a persistent trend towards larger vessel sizes over the decades. For instance, in the realm of container ships, vessel sizes have surged from under 10,000 to 24,000 TEU (twenty-foot equivalent unit). Presently, a larger class of container ships dominates three major container routes: Asia–Europe, Asia–North America, Europe–North America (Notteboom, 2020).

From a hydrodynamics perspective, ship motions are believed to be reduced for larger ships compared to smaller ones. Similar descriptions can be found in recent optimal ship routing studies. However, marine accidents continue to occur, such as the breakage of the 8110 TEU container ship, named “MOL Comfort,” in the Indian Ocean in 2013 involving the collapse of loaded containers on many container ships, including larger ones. Notably, the 14,000 TEU container ship, named “ONE Apus,” lost 1850 containers in the Pacific Ocean on a voyage from Asia to North America in November 2020 (Emergency Response Division, 2020). Container loss has been reported every year, with an average loss of 2301 containers per year over the last three years (2020–2022) (World Shipping Council, 2023). These accidents lead to environmental problems and economic losses.

The trend toward larger ships is evident not only in container ships but also in bulk carriers and tankers. According to ITF (International Transport Forum, 2015), the average ship size in deadweight tonnage (DWT) grew by 90% for container ships, 50% for bulk carriers, and 21% for tankers from 1996 to 2015. The number of very large ore carriers (VLOC), known as Valemax or Chinamax, has particularly increased to transport iron ore from Brazil to China (Papadionysiou, 2014). These ships can carry 400,000 tons in a single voyage, more than twice the capacity of 180,000 tons of Capesize bulk carriers. However, several incidents have been reported where large ships suffered multiple hull

* Corresponding author.
E-mail address: sasa@maritime.kobe-u.ac.jp (K. Sasa).

https://doi.org/10.1016/j.oceaneng.2024.119121
Received 13 June 2024; Received in revised form 26 August 2024; Accepted 27 August 2024
Available online 6 September 2024

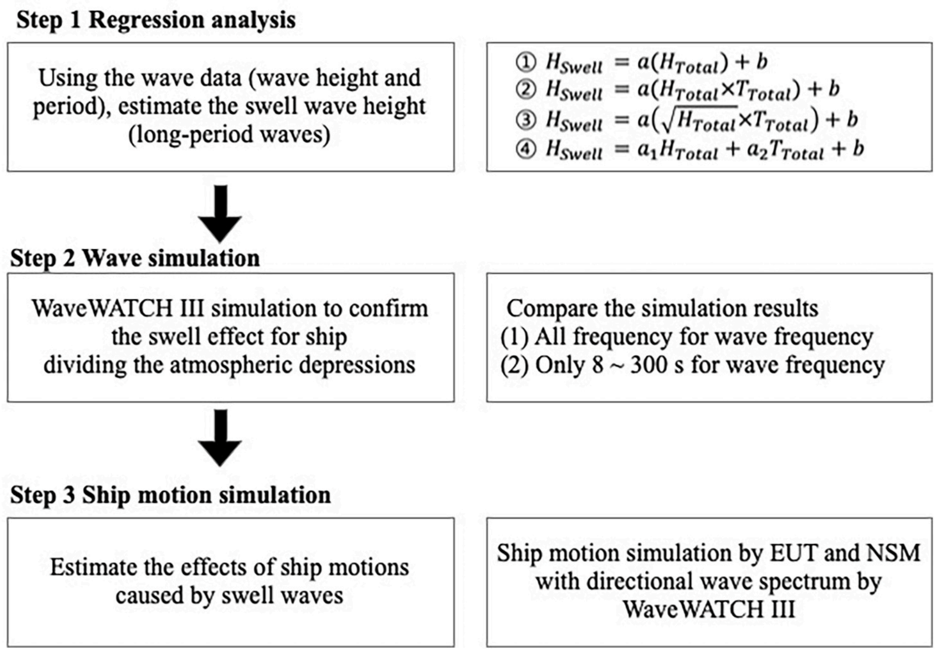

Fig. 1. Flowchart of this study.

cracks in rough waves (Safety4sea, 2012).

Understanding the properties of ocean waves is necessary to prevent accidents in open seas. Although many studies on ocean waves have been conducted for decades, most have focused on their wind-wave mechanisms. Ocean waves contain several wave components during different wave periods, such as swells and wind waves (Vincent et al., 2019). Villefer et al. (2023) evaluated spectral wave modeling by combining swells and wind waves to reproduce sea state conditions. Jiang et al. (2023) established a wave dataset from historical simulations and future scenarios in the form of swells and wind waves separately. Wind waves consist of irregular and short-crested waves and are strongly affected by wind variance. However, swell waves are more regular, have longer periods, and are not strongly related to wind.

Swell waves represent a significant risk factor for maritime operations. Numerous studies have demonstrated the operational challenges ships encounter owing to the presence of long-period waves. Specifically, the existence of long-period waves, typically lasting 1–2 min, renders ships moored in harbors vulnerable, particularly when exposed to open seas (Sakakibara and Kubo, 2008; Lopez and Iglesias, 2014; Sasa, 2017; Lee et al., 2021; Costas et al., 2022). Ship navigation is occasionally jeopardized by long-period waves lasting approximately 10–20 s, which induce substantial ship movements (Zhang and Li, 2017). These significant ship motions can compromise cargo lashing integrity, precipitating maritime accidents such as cargo lashing failures, container losses, and hull damage (Acanfora et al., 2017; Sasa et al., 2023). To mitigate the impact of rough seas on maritime activities, it is advisable to maintain a significant wave height below safety thresholds (Takashima et al., 2009; Grifoll et al., 2018; Sasa et al., 2021). However, relying solely on significant wave height as a criterion may overlook the effects of long-period waves, potentially leading to hazardous conditions.

Generally, atmospheric depressions are generated and developed in East Asia during the first stage in the North Pacific Ocean. Wind waves are generated if strong winds have been blowing for a prolonged period over a wide area. The wave heights and periods continue to develop as they mature. Once the wind waves mature, they propagate outside the atmospheric depressions, even without further energy input from the winds. The distance of propagation can exceed a couple of thousand kilometers in open seas, resulting in swell waves. The wave height of swell waves gradually decreases, and the wave period increases slightly as the propagation distance increases (Alves, 2006; Portilla et al., 2009). Swell waves are sometimes observed by ships offshore or by people in coastal zones and can become a severe threat in open seas such as the Pacific Ocean. Swell waves are known to have long wavelengths that are close to the length of ships and carry more energy than wind waves. This implies that ships should pay more attention to swell waves than to wind waves from a vibration theory perspective. In optimal ship routing, the basic idea is that a ship avoids atmospheric depressions caused by wind waves, as forecasted in weather reports. Recently, the European Center for Medium-range Weather Forecasts (ECMWF) has provided forecasted results for swell waves. However, the presence of swell waves is not yet fully integrated into optimal ship handling strategies. Determining the relationship between the development of atmospheric depressions, wind conditions, and wind waves may be necessary to construct optimal ship routing that also considers swell waves.

Various methods have been proposed for estimating wave information, including the wave buoy analogy (Nielsen, 2007, 2008; Iseki et al., 2013), marine radar (Carrasco et al., 2017; Ludeno and Serafino, 2019), draft meters (Terada et al., 2021), and drift buoys (Hirakawa et al., 2016), among others. However, no definitive method has emerged as suitable for estimating swell waves with practical accuracy. Consequently, several studies have focused on wave simulation to assess sea state. For instance, Chen et al. (2020) conducted wave simulations to identify the wind input sources capable of accurately reproducing sea-state conditions during severe weather. Similarly, Zheng et al. (2022) proposed a wave forecasting method based on the WaveWATCH III (WW3) model and an Artificial Neural Network (ANN). Despite the availability of swell wave height data in the fifth generation of ECMWF atmospheric reanalysis (ERA5), few studies have concentrated on numerically reproducing swell waves. Therefore, it is essential to delve into the detailed characteristics of swell waves that pose risks to ship operations, including their areas of generation, maturity, and propagation.

The height of swell waves is closely related to the significant wave height and wave period (Honda et al., 2013). This relationship stems from the characteristics of swell waves, which propagate and develop over long distances. Suganuma et al. (1995) validated this relationship by correlating the height of swell waves with significant wave height

Table 1
Initial conditions for case studies by wave simulation model.

Case	Wave condition	Wave frequency (period)		Wave direction	
		Range	Number	Range	Number
Case T	Total waves	0.0345–1.17 Hz (0.8–28.9 s)	38 frequencies	0–360°	36 directions
Case S	Swell waves Only	0.00313–0.125 Hz (8.0–319.5 s)	38 frequencies	0–360°	36 directions

Table 2
Main dimensions of the 63,000 DWT class bulk carrier.

Item	
Length between perpendicular lines	195.00 m
Breadth	32.24 m
Draft (fully loaded)	13.42 m
Voyage speed	13.70 knots

and mean wave period through measurements using wave buoys on the Japanese coast. However, applying these findings to ships engaged in ocean navigation is challenging because the correlation results were derived from coastal areas and did not encompass vast oceans such as the Pacific Ocean.

In this study, the relationship between swell waves and wind waves was analyzed using multiple regression formulas. This analysis elucidates the contribution of wave period, in addition to wave height, to the estimation of swell waves. Furthermore, the behavior of swell waves was numerically reproduced using a third-generation wave model.

The remainder of this paper is organized as follows: In Section 2, we elaborate on the data collection process and the methodology adopted for reanalyzing weather data, onboard measurements, wave simulation models, and ship motion models employed in this study. Section 3 delves into the estimation of swell waves utilizing regression models incorporating significant wave heights and mean wave periods. Through analysis, we elucidate the respective contributions of each factor to swell wave estimation. Finally, in Section 4, we provide a summary of the simulated results pertaining to the swell wave components corresponding to various types of atmospheric depressions. These results are compared with the total waves in ERA5, and their influence on the ship is evaluated by estimating ship motions. In Section 5, the estimated ship motions are compared with the measured motions in various wave cases to validate the reproduction of the swell waves. Section 6 evaluates the accuracy of the regression models for swell waves and discusses the accuracy of the estimated ship motions using wave simulation with a frequency response function. Finally, Section 7 summarizes the conclusions and suggests directions for future research.

2. Data collection and methodology

This section details the data collection and analysis methods employed to statistically and numerically estimate swell waves. The framework of this study consisted of three steps, as illustrated in Fig. 1. In the first step, the contribution of the wave period was compared for each regression formula to estimate swell waves. In the second step, the wave model reproduced the propagation of swell waves after the generation and maturation of wind waves in each type of atmospheric depression. Lastly, in the third step, the estimated swell waves were validated as ship motions using the measured data.

The collection of reanalysis weather data from ERA5 is detailed in Section 2.1. The wave simulation model employed to reproduce sea states under various conditions is summarized in Section 2.2. Section 2.3 describes the onboard measurements for the 63,000-DWT class bulk carrier utilized in this study.

2.1. Reanalysis of weather data from ERA5

Wave data were acquired from ERA5 provided by ECMWF to analyze swell wave information (Dee et al., 2011). ERA5 offers high-resolution hourly data at single levels, with a horizontal resolution of 31 km for atmospheric data (approximately 0.25°) and 62 km for ocean wave data (approximately 0.5°). Various climate datasets are available, but for this study, ERA5 reanalysis data were chosen because they provide output parameters separately for swell, wind, and combined total waves. Detailed information on the wave model can be found in the ECMWF documentation (ECMWF, 2021). Bruno et al. (2020) assessed the performance of the ERA5 wave model for swell waves using observed wave data, finding that the ERA5 wave model tended to overestimate swell wave heights. In this study, wind and wave data were collected, including the 10 m u-component (east–west direction) of wind, 10 m v-component (north–south direction) of wind, significant height of combined wind waves and swell, mean wave period, mean wave direction, significant height of total swell, mean wave period of total swell, and mean wave direction of total swell.

2.2. Wave simulation by WaveWATCH III

Many studies have utilized the WW3 model (version 4.18) as the third-generation phase-averaged wave model for wave hindcast simulations (Booij and Holthuijsen, 1987; Tolman, 1989, 2014). This model has been widely applied in ocean engineering and meteorology for various purposes. Among the National Centers for Environmental Prediction Final (NCEP-FNL) datasets (Kalnay et al., 1996), which offer various wind input sources for wave simulations. Additionally, the ECMWF reanalysis database (Dee et al., 2011) was introduced. The NCEP-FNL dataset was selected as the wind input because it has demonstrated high accuracy for ship motion in various studies (Chen et al., 2021; Lee et al., 2022; Sasa et al., 2023).

In this study, the WW3 model was utilized for two primary purposes: First, a wave simulation was conducted for all waves at all wave frequencies. However, the simulation was focused only on swell waves, thereby limiting the swell wave frequencies. The simulation settings for total and swell waves are listed in Table 1. The range of wave frequencies was set from 0.0345 to 1.17 Hz (0.8–28.9 s) for total waves and from 0.00313 to 0.124 Hz (8.06–320 s) for swell waves. The number of wave directions was set at 36, with intervals of 10°.

Second, wind, being the primary factor for wave generation, was input separately for each atmospheric depression to confirm wave development and propagation. Although simulations for each atmospheric depression differ from reproducing actual sea states, it appears feasible to validate the wave development process, including swell propagation, for each atmospheric depression.

A strong atmospheric depression originating in East Asia generates wind waves that propagate as swell waves passing through the North Pacific Ocean. In this study, the propagation of swell waves was estimated, and their distribution was confirmed through various wave simulation cases.

2.3. Onboard measurement

To determine the presence of swell waves, onboard measurements of a 63,000-DWT bulk carrier were conducted from April 2018 to November 2019. Table 2 summarizes the main dimensions of the bulk carrier. The bulk carrier navigated around the world without regular voyage routes, as depicted in Fig. 2.

The measured parameters encompass ship position, speed, heading, and rudder angle as navigation data; main engine speed, turbocharger speed, and scavenging air pressure as engine data; wind direction, wind speed, significant wave height, and mean wave period as weather data; and the pitch, roll, and yaw motions of the ship. Navigation and engine data were recorded every 1 s. They were transferred to a laptop from the

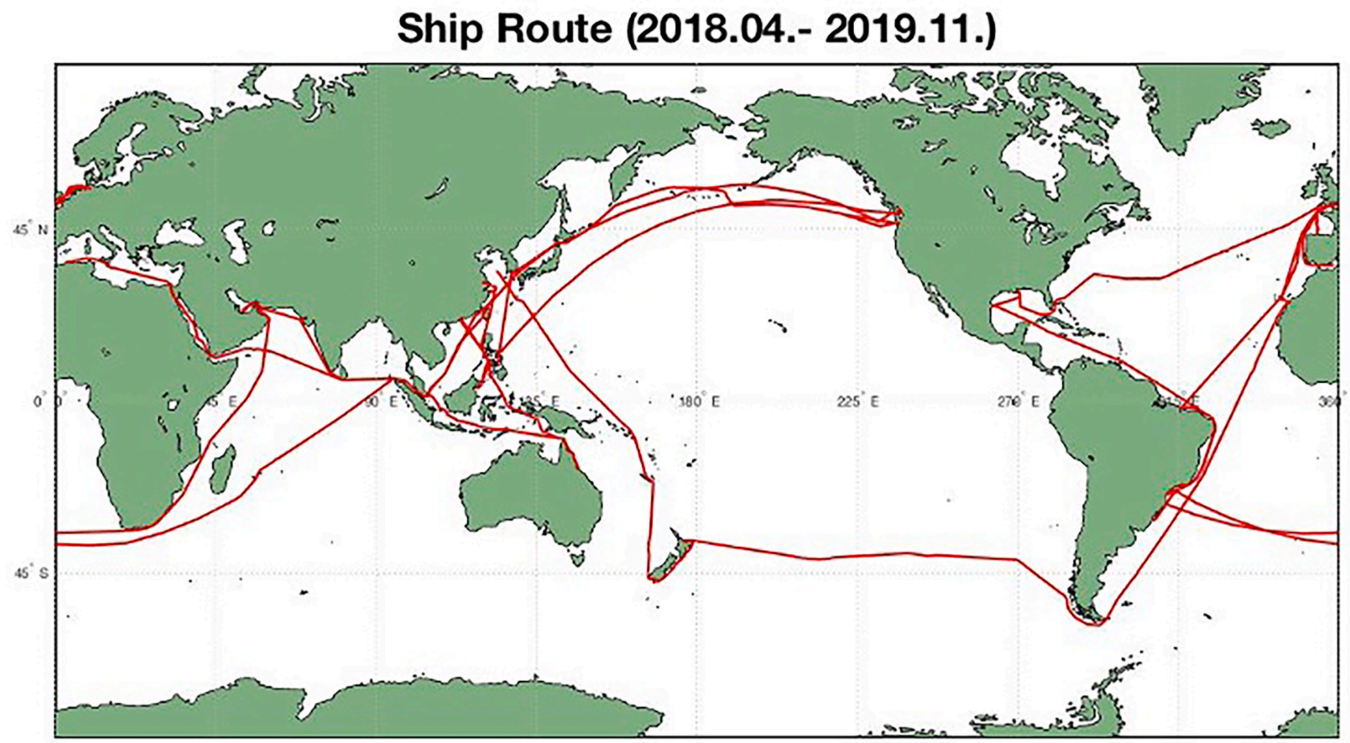

Fig. 2. Ship trajectory from April 2018 to November 2019.

Fig. 3. Wave radar analyzer installed in a bulk carrier.

Integrated Bridge Satellite System via a Voyage Data Recorder and the Engine Data Logger. An inertial measurement unit, NAV440, was installed on the ship bridge to measure the ship's roll, pitch, and yaw motions along with accelerations every 0.5 s. A wave radar analyzer was installed to estimate the wave condition using X-band radar, as shown in Fig. 3. Wave parameters, including wave height and period, were estimated utilizing this equipment. Notably, the use of wave radar has been widely studied (Carrasco et al., 2017; Ludeno and Serafino, 2019). However, its reliability as a definitive method for determining accurate values has not been firmly established. In particular, its accuracy has been shown to be insufficient in heavy rain or cloudy conditions. In this study, the wave radar data were used as part of the estimated results.

This study primarily focused on the impact of ship motion caused by swell waves. Hence, the collected data underwent analysis,

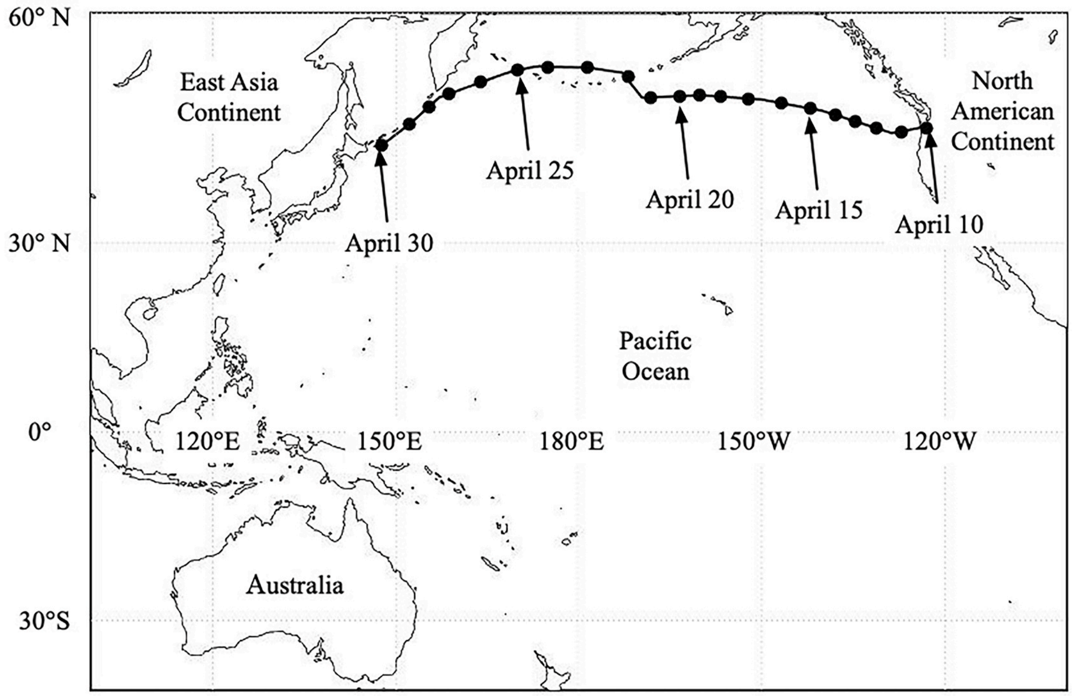

Fig. 4. Voyage route of the bulk carrier in April 2018.

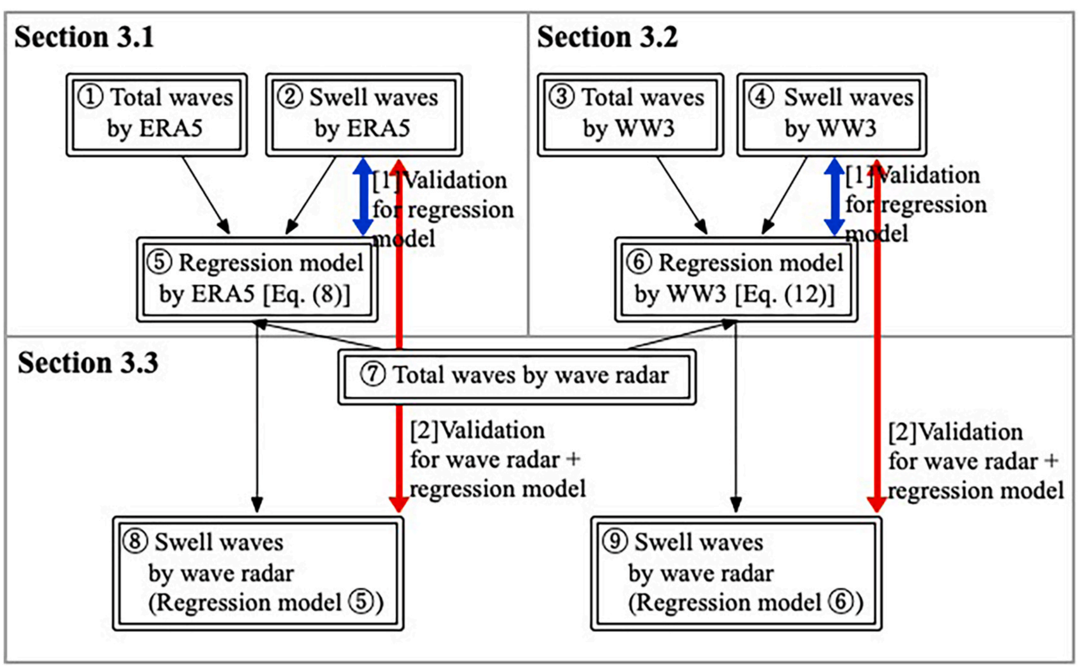

Fig. 5. Classification for each wave data in the regression model.

encompassing ship motion, navigational information, and weather parameters, complemented by ERA5 reanalysis data for ship position.

2.4. Estimating ship motions as validation of swell waves

Currently, there is no definitive method for wave observation in the ocean. Comparing the estimated ship motion with the measured motion remains a preferred approach (Lu et al., 2017; Waskito et al., 2022). While various seakeeping analysis models exist, the enhanced unified theory (EUT) (Kashiwagi, 1992, 1997) has been evaluated as a practically accurate model for real-world seas (Kashiwagi et al., 2004). Therefore, frequency response functions were computed using the EUT. The directional spectra for the pitch and roll motions can be estimated using Eqs. (1) and (2).

$$D_P(\omega,\theta,V) = \frac{|X_P(\omega,\theta,V)|^2}{\left|1-\dfrac{2\omega_0 V\cos\theta}{g}\right|} D_W(\omega_0,\theta), \tag{1}$$

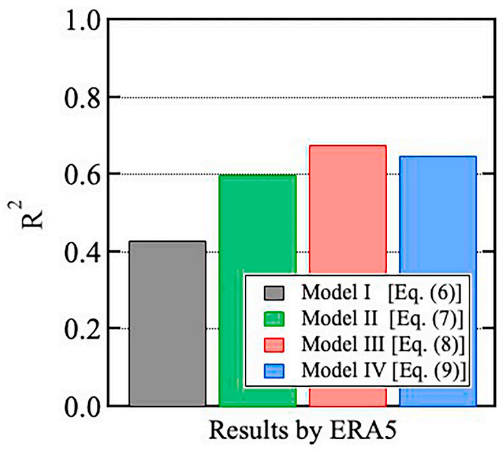

Fig. 6. Accuracy of regression models for the swell wave height by ERA5 data.

$$D_R(\omega,\theta,V) = \frac{|X_R(\omega,\theta,V)|^2}{\left|1 - \dfrac{2\omega_0 V \cos\theta}{g}\right|} D_W(\omega_0,\theta), \tag{2}$$

where $D_P(\omega,\theta,V)$ and $D_R(\omega,\theta,V)$ are the directional spectrum of pitch and roll motions in the encounter wave frequency of ω, relative wave direction of θ, and ship speed of V. $D_W(\omega_0,\theta)$ is the directional wave spectrum and ω_0 is wave frequency of incident waves. $X_P(\omega,\theta,V)$ and $X_R(\omega,\theta,V)$ are the frequency response functions of pitch and roll, respectively.

The results of the directional spectra of ship motions were used to estimate the significant amplitudes in the pitch and roll motions, $PA_{1/3}$, $RA_{1/3}$ as in Eqs. (3) and (4), respectively.

$$PA_{1/3} = 4.0\sqrt{\int_0^{2\pi}\int_0^{\infty} D_P(\omega,\theta,V)\,d\omega d\theta}, \tag{3}$$

$$RA_{1/3} = 4.0\sqrt{\int_0^{2\pi}\int_0^{\infty} D_R(\omega,\theta,V)\,d\omega d\theta}. \tag{4}$$

The estimated ship motions were compared under various case studies by wave simulation using the WW3 model as the directional wave spectrum in the frequency domain.

3. Regression analysis for swell waves

The significant wave height and wind speed are the primary factors in the simulation of optimal ship routing. Although the influence of long-period waves, such as swells, has been identified as the main cause of large ship motion, there are limitations to considering long-period waves. The estimation of swell waves has conventionally relied on empirical methods (Phillips and Banner, 1974), and some studies have explored swell waves using high-frequency radar (Alattabi et al., 2019). Honda et al. (2013) proposed a regression formula to estimate long-period wave heights using significant wave height and mean wave period. However, this method has only been validated in a limited number of areas along the Japanese coast, thus restricting its applicability in wide oceans such as the Pacific Ocean. The data analysis was

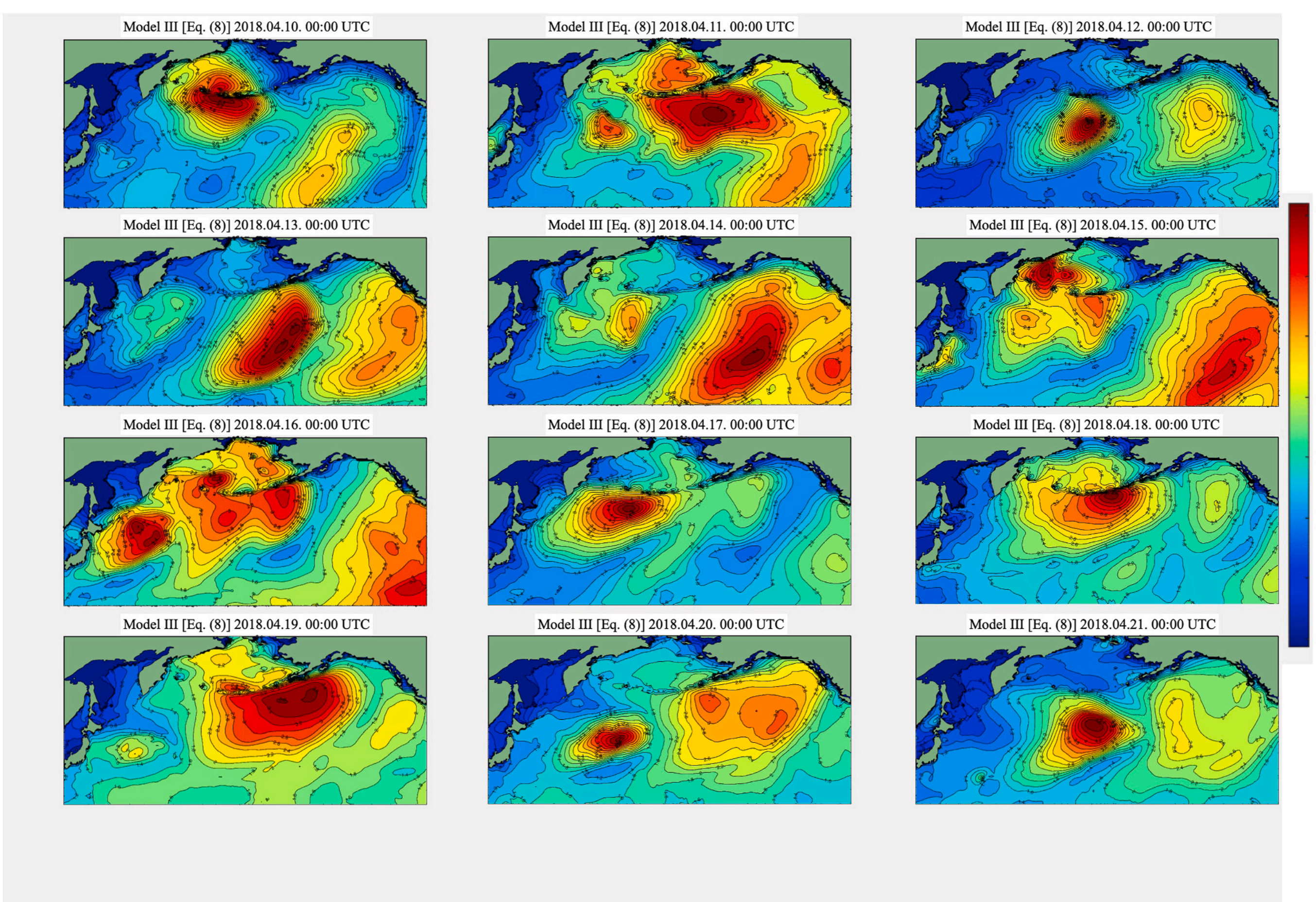

Fig. 7. Distribution of estimated swell waves using Model III [Eq. (8)].

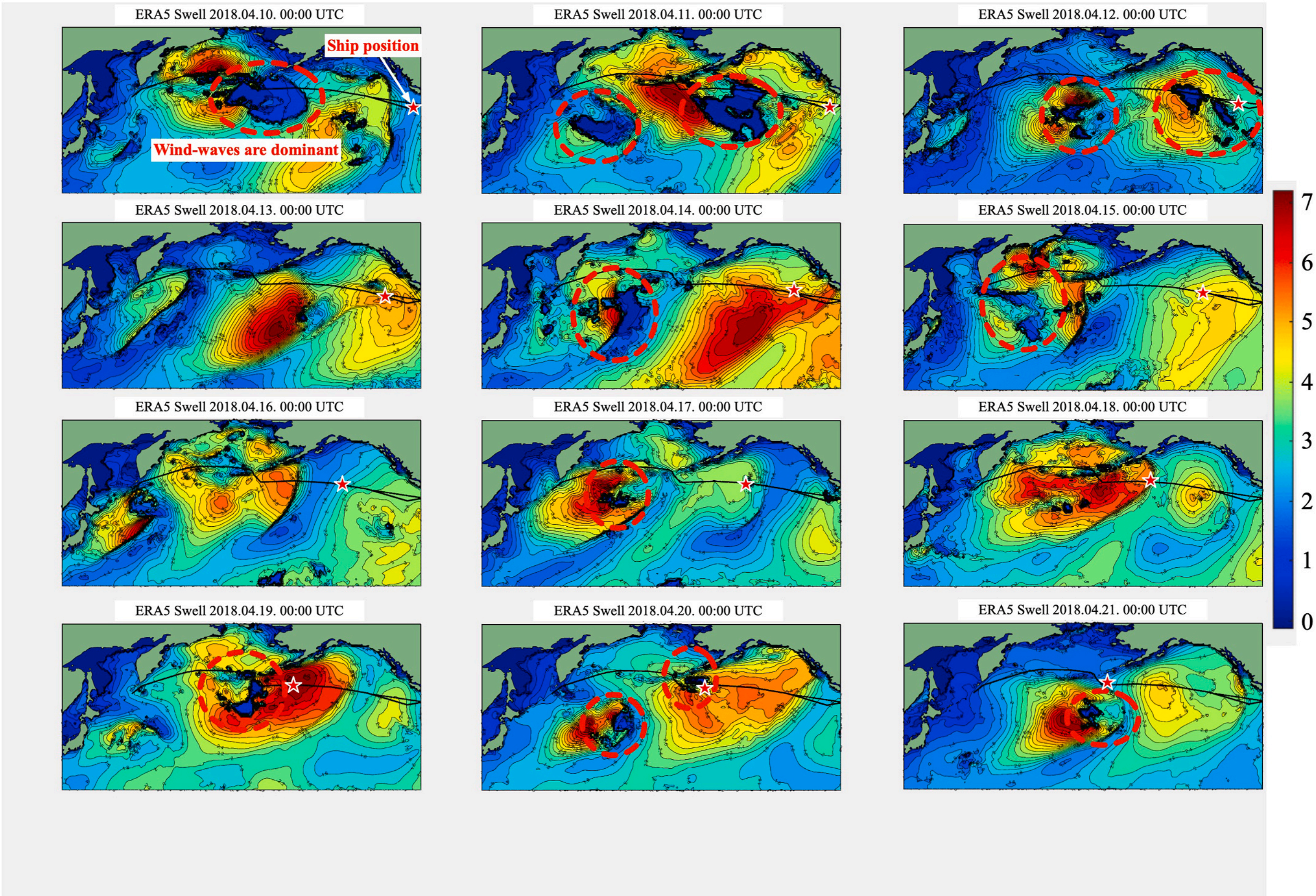

Fig. 8. Distribution of original swell waves from ERA5 data.

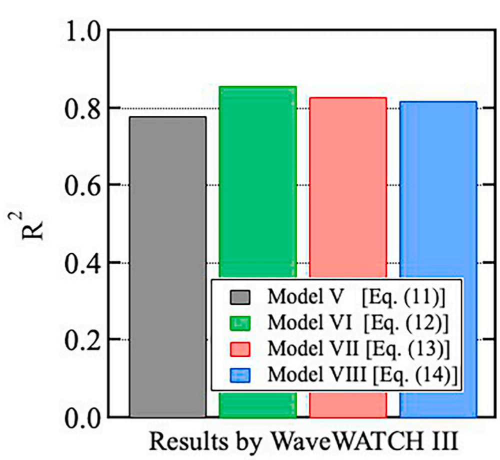

Fig. 9. Accuracy of regression models for the swell wave height using WW3 simulation results.

conducted during the period of voyage from North America to East Asia in April 2018 as shown in Fig. 4.

In this section, a regression analysis encompassing ocean and coastal waters was conducted to estimate swell wave height using significant wave height and mean wave period. To clarify the wave data from various sources in this study, each wave dataset is defined as shown in Fig. 5. Additionally, the estimated wave data presented in this section are validated. In 3.1, ERA5 reanalysis data (①, ② in Fig. 5) are utilized for regression analysis (⑤ in Fig. 5). Section 3.2 presents the regression analysis (⑥ in Fig. 5) using wave simulation results (③, ④ in Fig. 5). Subsequently, in 3.3, swell waves are estimated at the ship's location (⑧, ⑨ in Fig. 5) with the regression formulas from 3.1 to 3.2, applying the wave height and wave period obtained from wave radar (⑦ in Fig. 5).

3.1. Swell waves using ERA5 reanalysis data

As previously mentioned in Introduction, long-period waves (approximately 1–2 min) play a crucial role in the safety assessment of moored ships. Spectral analysis is indispensable for evaluating the height of these long-period waves. Some regression analysis studies attempt to estimate this parameter solely based on significant waves. In this study, we construct four types of regression models, serving as a reference to earlier works (Hiraishi et al., 1997), for estimating the wave height of swell waves. These models utilize significant wave height and mean wave period, as depicted in Eq. (5). Model I represents a linear equation that solely considers wave height. Model II introduces a linear equation incorporating the product of wave height and period. Model III uses the product of the root of the wave height and wave period. Lastly, Model IV comprises a multi-regression model utilizing both wave height and period.

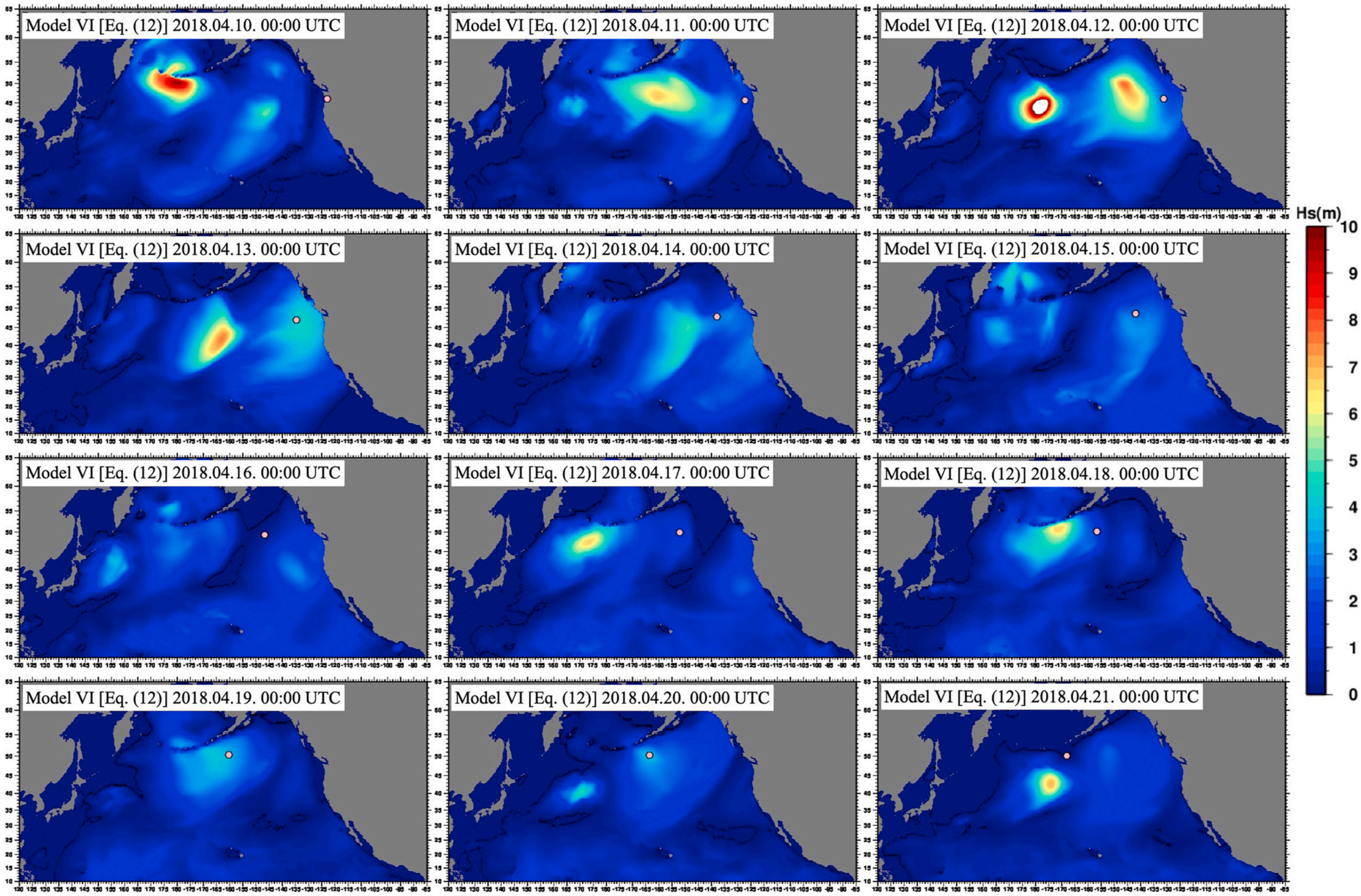

Fig. 10. Distribution of swell waves using Model VI [Eq. (12)].

Model Number	*Model Equation*
I	$H_{Swell} = \alpha_1(H_{Total}) + \beta_1$
II	$H_{Swell} = \alpha_2(H_{Total} \times T_{mean}) + \beta_2$
III	$H_{Swell} = \alpha_3\left(\sqrt{H_{Total}} \times T_{mean}\right) + \beta_3$
IV	$H_{Swell} = \alpha_4(H_{Total}) + \beta_4(T_{mean}) + \gamma_4$

(5)

where H_{Swell} is the significant wave height of the swell component and H_{Total} is the significant wave height of the combined wind waves and swell waves. T_{mean} is the mean wave period of the combined wind and swell waves. α_1, α_2, α_3, α_4, β_1, β_2, β_3, β_4, and γ_4 are the corresponding regression coefficients for each equation. These coefficients are obtained by the wave information of ERA5 (①, ② in Fig. 5) in the range of 25–65 N ° and 135 E−125 W ° in April 2018. The results of Models I–IV are expressed in Eqs. (6)–(9).

$$H_{Swell} = 0.54(H_{Total}) + 0.74, \tag{6}$$

$$H_{Swell} = 0.05(H_{Total} \times T_{mean}) + 0.88, \tag{7}$$

$$H_{Swell} = 0.16\left(\sqrt{H_{Total}} \times T_{mean}\right) - 0.01, \tag{8}$$

$$H_{Swell} = 0.33(H_{Total}) + 0.30(T_{mean}) - 1.25. \tag{9}$$

The accuracy of each regression model was compared using R^2, the coefficient of determination in Eq. (10).

$$R^2 = 1 - \frac{\sum_{i=1}^{N}(\widehat{y}_i - y_i)^2}{\sum_{i=1}^{N}(\widehat{y}_i - \overline{y})^2}, \tag{10}$$

where $\widehat{y}_i$ is the predicted value, y_i is the hindcast value, and N is the amount of input data. Fig. 6 displays the accuracy of the regression models utilizing ERA5 data. Model III [Eq. (8)] demonstrated the highest score, approximately 0.7, while Model IV [Eq. (9)] can be employed to estimate the swell wave height with an R^2 of approximately 0.65.

Fig. 7 depicts the distributions of the swell waves estimated using Eq. (8) for the North Pacific in April 2018 (marked as ⑤ in Fig. 5). Meanwhile, Fig. 8 illustrates the distribution of the swell waves drawn from ERA5 reanalysis data (marked as ② in Fig. 5). The overall patterns in Figs. 7 and 8 exhibit similarities, suggesting that the regression model accurately estimates the swell waves. However, some discrepancies were observed in the regression model, particularly in areas dominated by wind waves, as indicated by the dotted red circles in Fig. 8. These characteristics of swell waves from ERA5 resulted in the low accuracy and quality of the presented regression models, indicating a swell height of nearly 0 in areas dominated by wind waves. However, in other sea areas, the estimations were accurate, as shown in Figs. 7 and 8. In addition, the target ship was not in an area where wind waves are dominant, as marked by the red stars in Fig. 8. Therefore, the regression models could accurately estimate the swell waves in the ship position.

3.2. Swell waves using simulated results of WW3

The regression models were further developed using the simulated results of WW3 (marked as ③ and ④ in Fig. 5) for April 2018. As mentioned, two simulation cases were conducted: Case T covering the range of 0.8–28.9 s and Case S spanning from 8.0 to 320.0 s as outlined in Table 1. The regression models for these simulation results were derived using Eqs. (11)–(14).

$$H_{Swell} = 1.00(H_{Total}) - 1.98, \tag{11}$$

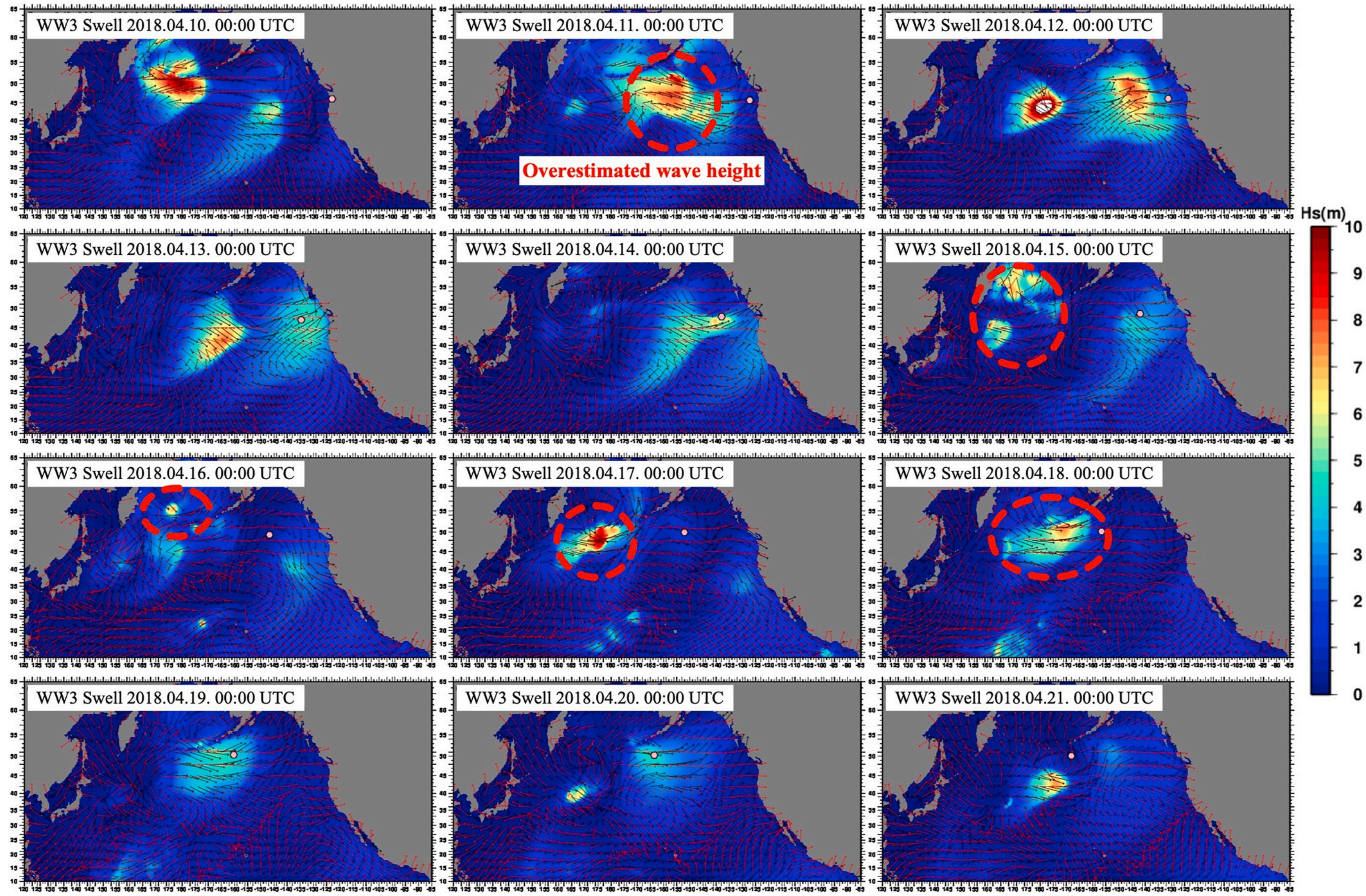

Fig. 11. Distribution of swell waves reproduced by WW3.

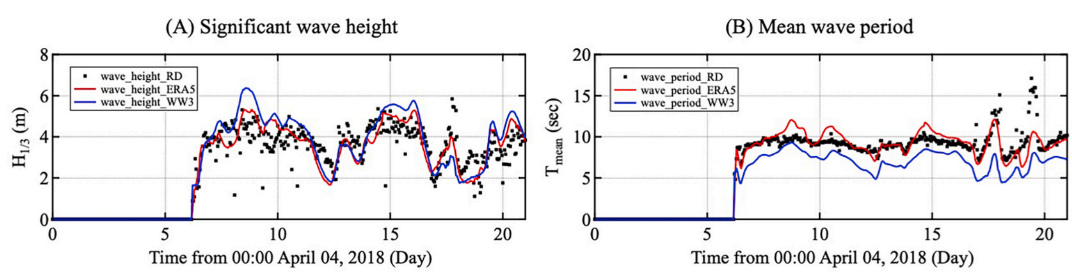

Fig. 12. Comparison of wave height and period at the ship's position obtained from the wave radar analyzer, ERA5 reanalysis data, and WW3 simulation results.

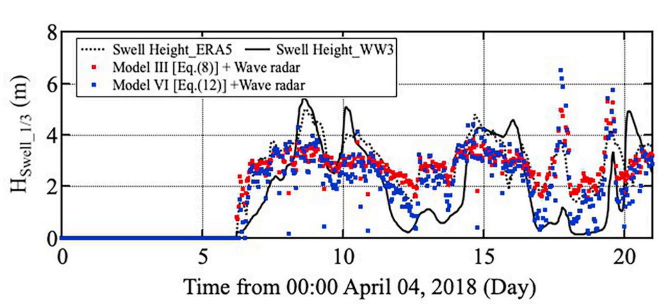

Fig. 13. Comparison of variations in swell waves in ship positions.

$$H_{Swell} = 0.10(H_{Total} \times T_{mean}) - 1.04, \tag{12}$$

$$H_{Swell} = 0.32\left(\sqrt{H_{Total}} \times T_{mean}\right) - 2.61, \tag{13}$$

$$H_{Swell} = 0.74(H_{Total}) + 0.43(T_{mean}) - 3.99, \tag{14}$$

Fig. 9 shows the results of comparing the coefficient of determination R^2 for each model. In contrast to the regression models utilizing ERA5 reanalysis data, Model VI [Eq. (12)] exhibited good accuracy (R^2 = 0.86).

Fig. 10 illustrates the estimated distribution of the swell waves using Model VI [Eq. (12)] for the North Pacific in April 2018 (marked as ⑥ in Fig. 5). Meanwhile, Fig. 11 displays the distribution of the swell waves simulated by WW3 for Case S (marked as ④ in Fig. 5). A comparison between Figs. 10 and 11 reveals that Model VI [Eq. (12)] accurately estimates the swell waves, except at certain points. The results indicate that the swell waves propagated more extensively outside the

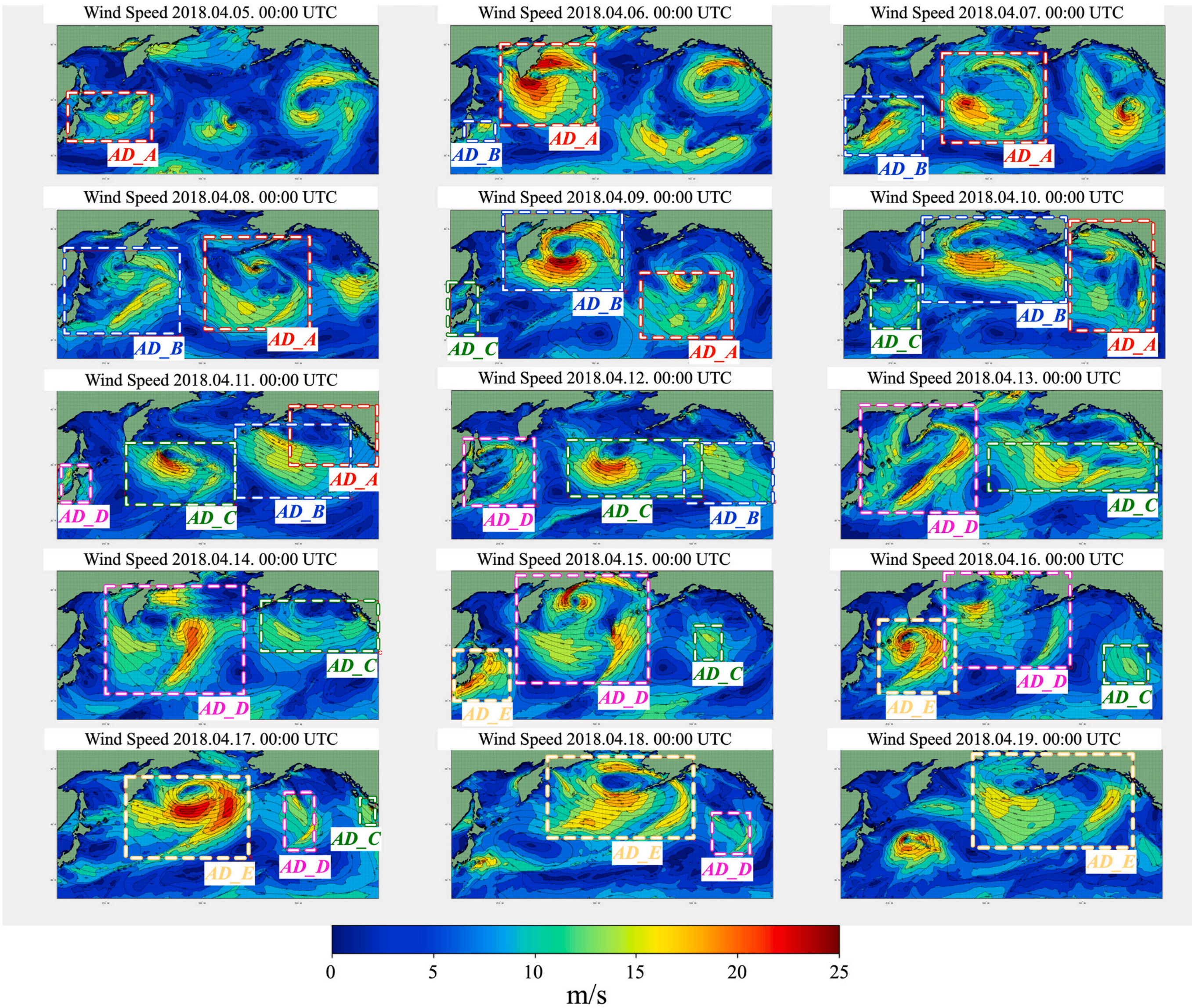

Fig. 14. Distribution for wind speed separated by atmospheric depression A–E.

atmospheric depression, while the numerical simulation results tended to overestimate the center of the peak waves. These parts are marked with dotted red circles in Fig. 11. This implies that the peak wave height was underestimated when the regression models were used.

3.3. Application for measured waves

In this section, the aforementioned regression models are applied to the wave height and period data collected by a wave radar to estimate the swell wave height. As previously stated, the accuracy of the wave radar measurements is not deemed reliable as a true value, and it lacks the capability to estimate swell waves. In Section 3.1, Model III [Eq. (8)] demonstrated the highest accuracy using the ERA5 reanalysis data, while in Section 3.2, Model VI [Eq. (12)] utilizing the simulated results proved to be the most accurate. By employing these two regression models, the swell wave height was estimated by integrating the wave data from the wave radar. Fig. 12 presents a comparison of the significant wave height and mean wave period at the ship position obtained from the wave radar (marked as ⑦ in Fig. 5), ERA5 reanalysis data, and WW3 simulation results. In the figure, the wave height and period obtained from the wave radar are denoted by black dots, while the ERA5 reanalysis data and wave simulation results are represented by red and blue lines, respectively.

Fig. 13 presents a comparison of the swell waves obtained from each method. The black dotted and solid lines represent the swell height derived from ERA5 reanalysis data (marked as ② in Fig. 5) and wave simulation results (marked as ④ in Fig. 5), respectively. Meanwhile, the red and blue dots denote the estimated swell waves by the regression models (marked as ⑧ and ⑨ in Fig. 5) using Eqs. (8) and (12), respectively.

As depicted in Fig. 13, the swell waves derived from both the regression formulas combined with wave radar data (marked as ⑧ and ⑨ in Fig. 5) exhibit a similar pattern to other data sources. Despite accurately capturing the pattern of swell waves, these regression models display some errors. Specifically, they tend to overestimate the peak wave height over a period of 15–20 d. This discrepancy could be attributed to the inaccuracies inherent in the wave radar measurements.

4. Wave simulation for separated by atmospheric depression

Given that existing wave simulations aim to replicate real sea conditions, input data such as air pressure, wind speed, and direction need to be sourced from information closely resembling the actual scenario. However, our approach was focused on identifying the generation of

Table 3
Simulation case separated by atmospheric depression A–E and wave frequencies.

Case	Input of atmospheric depression	Period of effect (UTC)	Wave frequency (period)
Case T-0	All	2018.04.04.00:00–2018.04.25.00:00	0.0345–1.17 Hz (0.8–28.9 s)
Case T-A	AD A	2018.04.04.06:00–2018.04.11.00:00	
Case T-B	AD B	2018.04.05.18:00–2018.04.12.06:00	
Case T-C	AD C	2018.04.09.00:00–2018.04.17.00:00	
Case T-D	AD D	2018.04.11.00:00–2018.04.18.00:00	
Case T-E	AD E	2018.04.14.12:00–2018.04.21.00:00	
Case S-0	All	2018.04.04.00:00–2018.04.25.00:00	0.00313–0.125 Hz (8.0–319.5 s)
Case S-A	AD A	2018.04.04.06:00–2018.04.11.00:00	
Case S-B	AD B	2018.04.05.18:00–2018.04.12.06:00	
Case S-C	AD C	2018.04.09.00:00–2018.04.17.00:00	
Case S-D	AD D	2018.04.11.00:00–2018.04.18.00:00	
Case S-E	AD E	2018.04.14.12:00–2018.04.21.00:00	

wind waves and propagation of swell waves induced by specific atmospheric depressions. This entailed having wind input concentrated solely near each respective atmospheric depression while setting. This implies that the wind input was set to zero in other areas. Five cases of rough seas were caused by atmospheric depressions in the North Pacific in April 2018 in Section 4.1. The results of the simulated waves are compared for individual atmospheric depressions at all wave frequencies in Section 4.2. Wave simulations were exclusively conducted for the frequencies pertinent to swell waves, as detailed in Section 4.3.

4.1. Atmospheric depression case (A–E case study)

The atmospheric depression cases were categorized into five conditions, designated as atmospheric depressions A through E (AD A–E), as depicted in Fig. 14 and Table 3. Atmospheric depressions are known to produce robust winds and waves. These wind waves propagate and evolve into swell waves across the Pacific Ocean.

Wave simulations were conducted with the identified atmospheric depression, wherein input winds were applied solely within the respective areas during the period of wind influence, as delineated in Fig. 14 and Table 3. In each case, the minimum air pressure was approximately 970 hPa, and the maximum wind speed reached approximately 30 m/s. These weather conditions resulted in the ship encountering various rough wave conditions.

4.2. Simulated results for waves in all frequencies

In Section 4.2, wave simulations were conducted to replicate the total wave conditions, encompassing both wind-generated and swell waves. Six types of wind conditions were defined, as outlined in Table 3: cases T-0, T-A, T-B, T-C, T-D, and T-E. Fig. 15 illustrates the reproduced distribution of wave heights and wave directions with the wind vectors as input (Case T-0). Notably, multiple strong waves were observed during this period. The distribution of wave heights suggests a propagation of waves from East Asia to the North Pacific Ocean, with no discernible results in the opposite direction.

Fig. 16 provides a comparison between the simulated results and ERA5 reanalysis data for the ship's position. While the significant wave height was well-replicated, the simulated mean wave periods consistently appeared to be smaller by 2–3 s than for the ERA5 reanalysis data.

Wave simulations were executed utilizing various wind inputs to observe each atmospheric depression characterized by strong winds. The simulation outcomes reveal a distinct wave field originating from each atmospheric depression in the Pacific Ocean. These results are depicted in Appendix 1, illustrating each case of AD A–E (Case T-A–T-E).

Fig. 17 displays the variations in wave heights attributable to a single atmospheric depression at the ship's position. These figures demonstrate that the wave simulations can accurately portray wave distributions resulting from a solitary atmospheric depression. It is evident that each wave height closely resembles that depicted in the ERA5 reanalysis data and simulated results, as illustrated in Fig. 17. The peak values of the wave height were accurately estimated even when considering the wind vector originating from a single atmospheric depression. Minimal discrepancy was observed between the results of the total wave simulation (depicted by the black solid line). This suggests that each wave was predominantly influenced by a singular atmospheric depression.

4.3. Simulated results for swell wave components

In this section, additional wave simulations were conducted solely to replicate swell waves, with the frequency range defined as 0.00313–0.125 Hz, as detailed in Table 3. Under this setup, swell waves could be reproduced within the range of 8–320 s. Six case studies were delineated for swell waves, listed as Cases S-0, S-A, S-B, S-C, S-D, and S-E.

Fig. 18 shows the distribution of swell waves with limited frequencies when considering all winds (Case S-0). Here, the wave height is marginally reduced compared to that depicted in Fig. 15 (Case T-0), indicating the exclusion of wind waves from consideration.

Fig. 19 illustrates the variations in the wave simulation results for swell waves compared with swell waves using the ERA5 reanalysis data at the ship's position. The wave height seems to be well-reproduced with minor discrepancies. However, there is a tendency for underestimation around days 13 and 14 as well as 17 and 18. Although the simulated results exhibit similarity in terms of the wave period, the peak period appears to be thrice that observed in the ERA5 reanalysis data, indicating a substantial difference. These discrepancies may have arisen owing to variations in settings between the ERA5 reanalysis and the wave simulations.

Subsequently, wave simulations were conducted specifically for swell waves associated with individual atmospheric depressions from Cases S-A to S-E, as outlined in Table 3. The outcomes of these simulations are depicted in Appendix 2.

Fig. 20 illustrates the results of the simulation of swell waves for each atmospheric depression alongside the ERA5 reanalysis data for the ship's position. It indicates that the swell waves were reproduced with minimal variation under each condition. Particularly noteworthy is the accurate estimation of the peak values of the swell waves in each atmospheric depression. Throughout this period, strong swell waves, reaching approximately 5 m in height, approached the ship three times. These occurrences were observed on days 7 and 8, 10 and 11, and 14 and 16, respectively, aligning with the peak waves in Cases S-B, S-C, and S-E.

5. Estimation of ship motions by directional wave spectrum and frequency response functions

In Section 4, various cases of wave simulation were conducted,

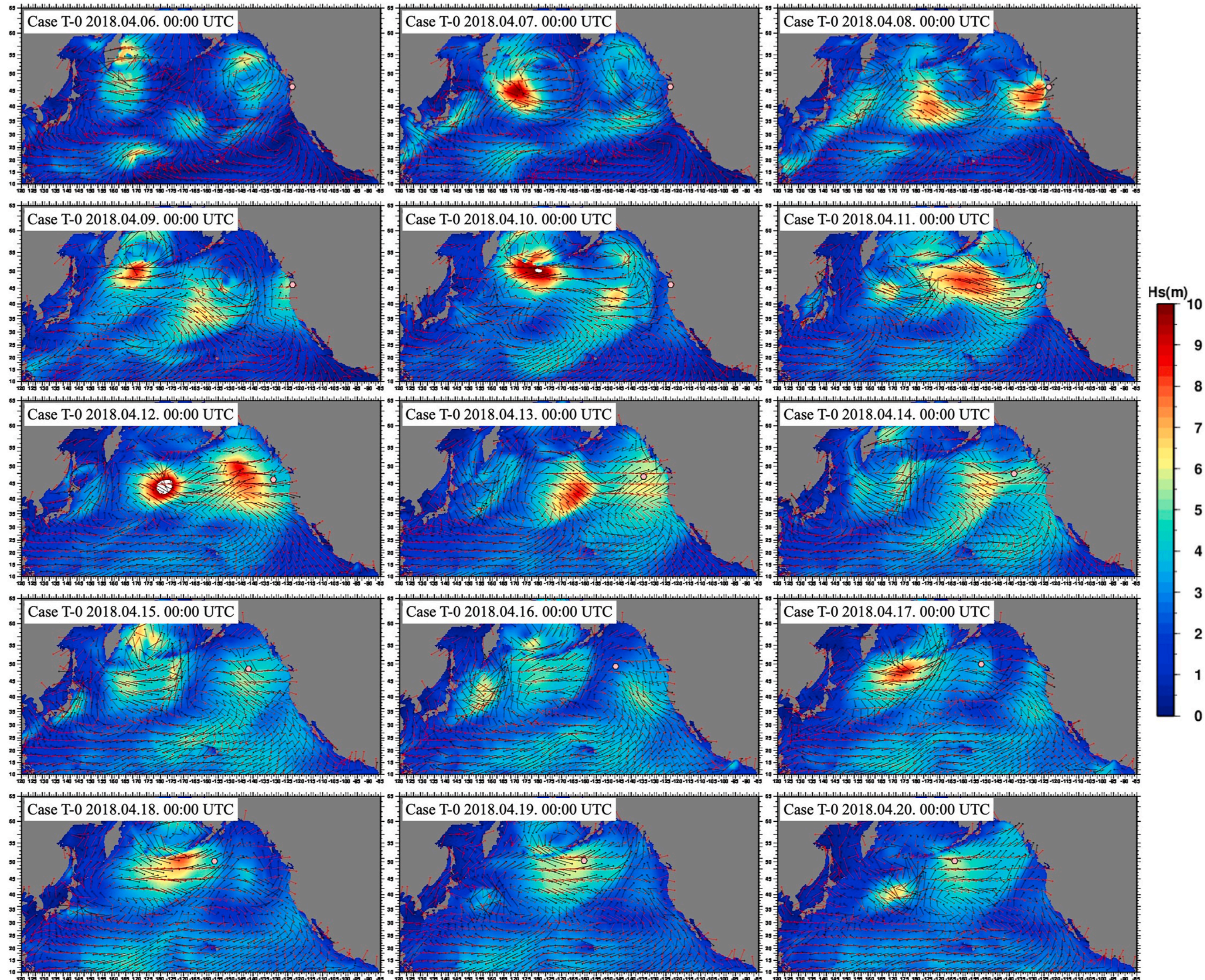

Fig. 15. Distribution for the simulated wave height for all frequencies (Case T-0).

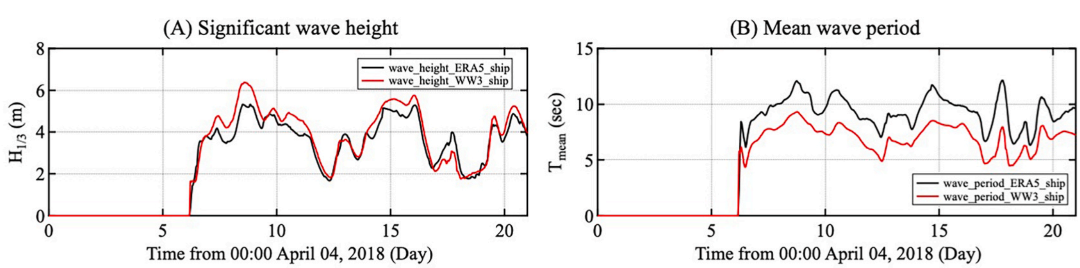

Fig. 16. Variations in wave simulation results for all waves in ship position.

categorizing total waves and swell waves and summarizing the effects of each atmospheric depression. In this section, the estimation and comparison of ship motions under simulated wave conditions are performed using the frequency response function and the EUT model outlined in Section 2.4.

It is noted here that the wave radar cannot be considered accurate as the true value in the validation process. This is primarily due to the lack of established standards for ocean-wave measurements. Although the simulated results were compared with the ERA5 reanalysis data, it should be acknowledged that the reanalysis data are not yet universally accepted as true values. However, ship motion measurements are relatively more reliable compared to ocean-wave measurements. Lu et al. (2017) demonstrated a validation methodology for estimated ship motions using onboard measurement data. In Section 5.1, the wave spectrum data for all wave frequencies obtained from Section 4.2 are utilized. In Section 5.2, the wave spectrum data for swell waves obtained from Section 4.3 are used to estimate the ship motions.

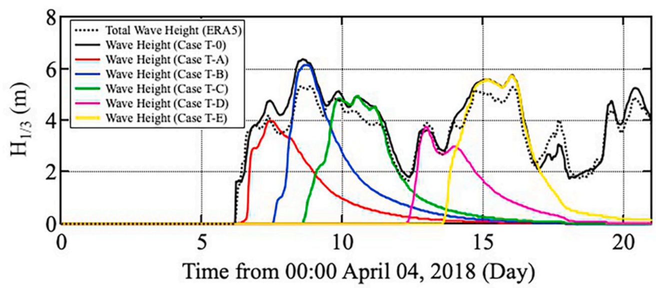

Fig. 17. Variations in wave height separated by AD A–E in ship position.

5.1. Simulated results in all frequencies

The significant ship motion amplitude was estimated using the directional wave spectrum and frequency response function. The directional wave spectrum was derived from wave simulations conducted for all wave frequencies in Section 4.2. Fig. 21 shows the sample directional wave spectrum when the swell waves were dominant at the ship position. It indicates that the ship encountered low-frequency, strong swell waves, with a peak frequency of approximately 0.07 Hz in the west direction. Based on these spectra, the surface elevation can be estimated as shown in Fig. 22, suggesting that high waves may have considerably affected the ship during this period.

Along with the wave spectrum, the pitch motion spectrum for measured ship motions is provided in Fig. 23. Evidently, the peak frequency of both pitch motion and waves is approximately 0.07–0.08 Hz, corresponding to a period of 12–14 s. Fig. 24 presents the measured pitch motions as time series data, showing that pitch motions within approximately 2°–6° occurred because of the influence of waves. The shape of the wave spectrum indicates that a wide range of waves affected the ship motions on April 14, potentially causing significant ship movements.

Subsequently, the estimated ship motions were compared with the measured ship motions, as depicted in Fig. 25. The ship predominantly encounters waves in the direction of the head sea, resulting in dominant pitch motion. Therefore, the accuracy of estimation for swell waves was evaluated based on pitch motion.

Fig. 25 illustrates that the estimated pitch motion closely resembled the measured motion. The maximum pitch motion was estimated to be approximately 4.5°, while the measured pitch motion was 4.8°.

Subsequently, ship motions were estimated using the wave simulation results for each atmospheric depression across all wave frequencies.

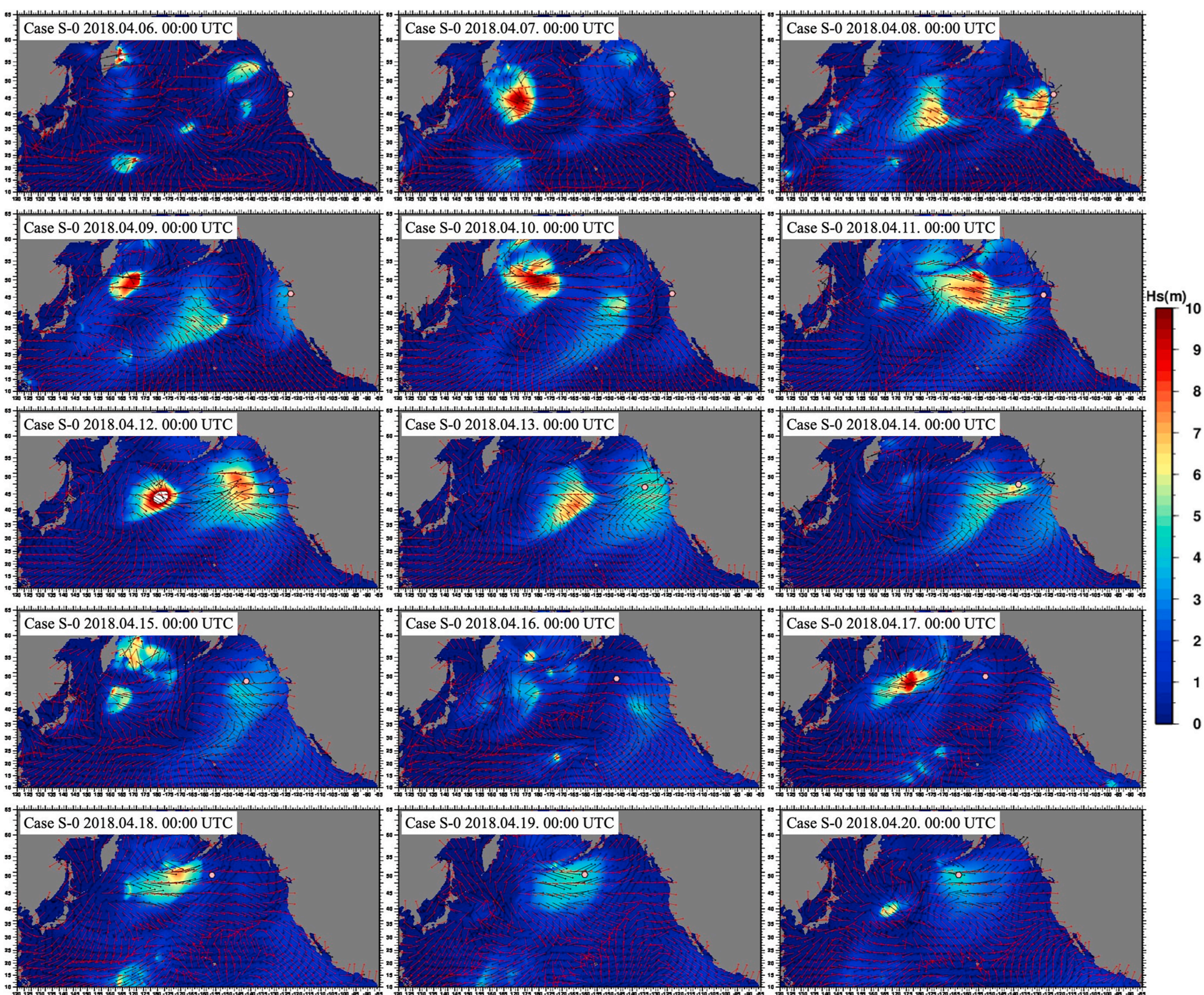

Fig. 18. Distribution for simulated wave height for swell wave components (Case S-0).

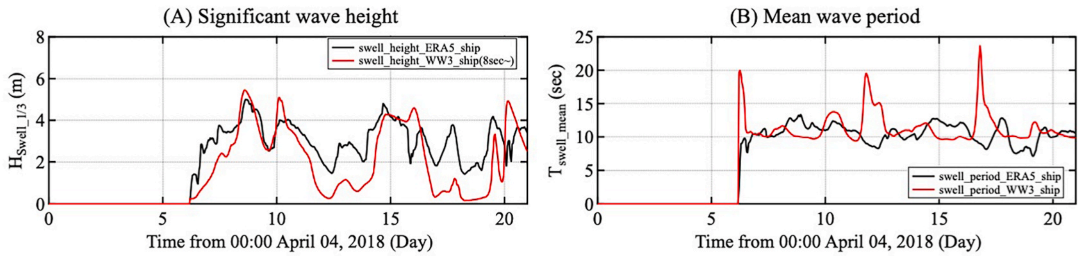

Fig. 19. Variations in wave simulation results for swell wave components in ship position.

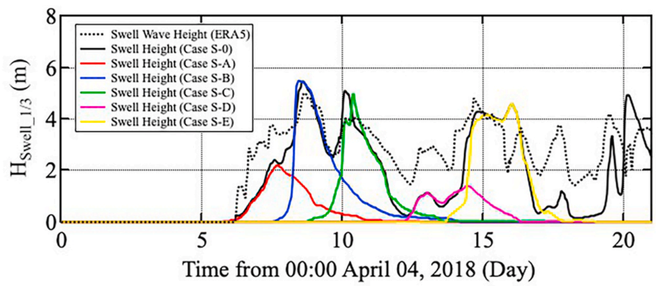

Fig. 20. Variations in wave height separated by AD A–E for swell wave components in ship position.

As depicted in Fig. 26, the estimated ship motions exhibited minimal deviation from the results encompassing all atmospheric depressions. These estimated ship motion results follow a similar trend as the simulated wave height results depicted in Fig. 17. This suggests that the method is effective for characterizing strong atmospheric depressions. While some errors were noted, the estimated motions agreed with the measured motions with practical accuracy.

The measured pitch motion displayed multiple peak values, with each peak value corresponding to the estimated pitch motion for each atmospheric depression. Despite slight underestimation observed during days 13–17, overall, the ship motion could be estimated with good agreement between the measured and estimated values.

5.2. Simulated results in only swell waves

In Section 5.2, ship motions are estimated using the simulated directional spectra of swell waves from Section 4.3. The frequency response function, computed using the EUT model, was applied to estimate the ship motions.

Fig. 27 illustrates the variations in the estimated ship motions attributed to swell waves compared with the measured data. The ship motions closely align with those depicted in Fig. 25. This suggests that ship motion primarily arises from swell waves.

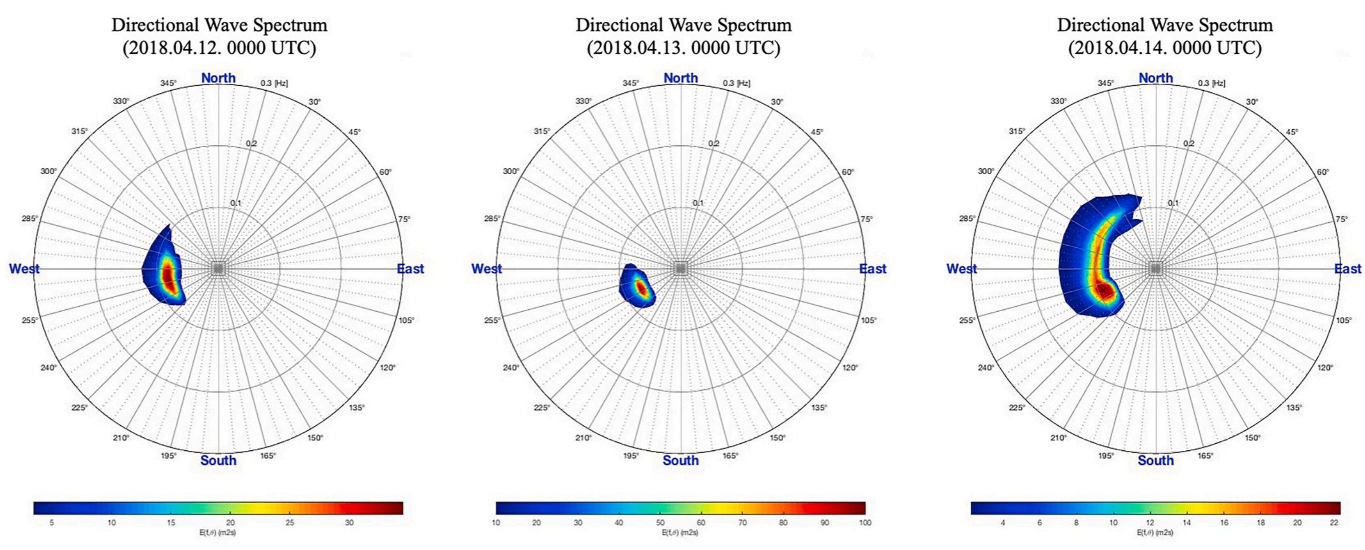

Fig. 21. Directional wave spectrum in ship position.

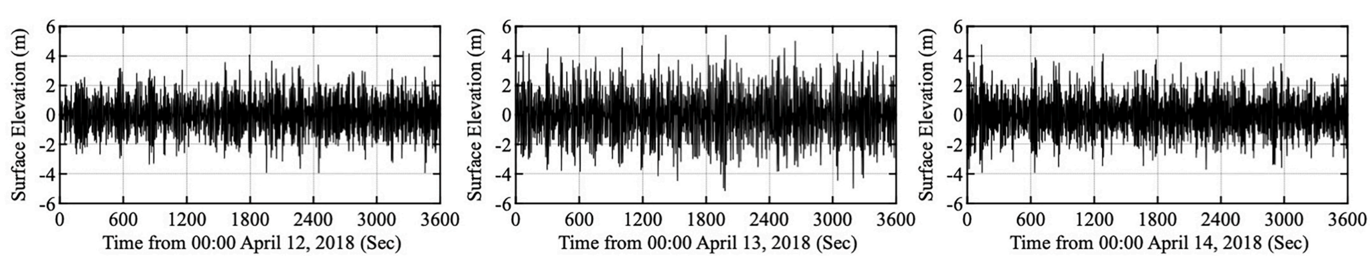

Fig. 22. Time series of wave surface elevation in ship position.

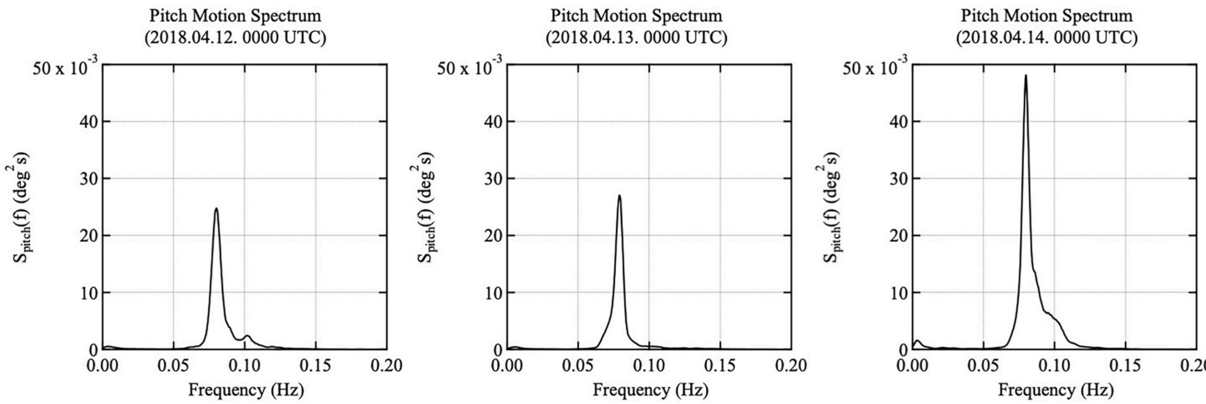

Fig. 23. Motion spectrum of pitch ship motions.

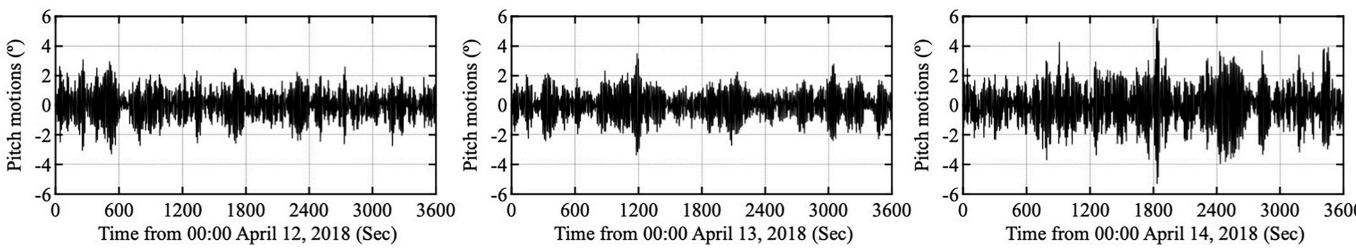

Fig. 24. Time series of pitch ship motions.

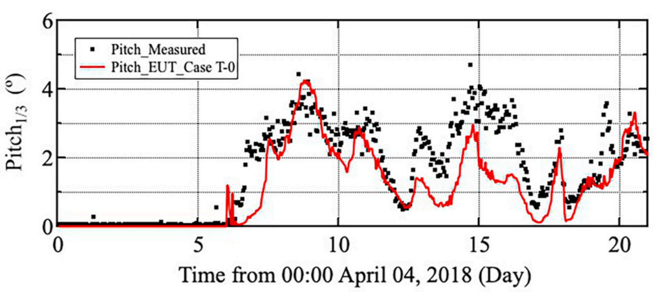

Fig. 25. Variations in ship motions in all wave frequencies.

Following that, ship motions were estimated using the wave simulation results for each atmospheric depression at the frequencies of the swell waves. Fig. 28 illustrates the variations in ship motion under these conditions. Despite slight underestimation in the swell waves, the simulated ship motion results closely agree with the measured ones. Furthermore, the ship motions for each atmospheric depression closely match the measured ship motions at the peak values. This indicates the dominant influence of swell waves on ship motion. Additionally, it is evident that each swell wave propagates independently from each atmospheric depression, ultimately affecting the ship motions.

6. Results and discussions

In this section, the accuracy of the regression models for swell waves from Section 3 is discussed, and the accuracy of the estimated ship motions from Section 5 is evaluated. The evaluation of each model's accuracy is based on the mean bias error (MBE) and root mean square error (RMSE). A brief overview of the standard metrics for MBE and RMSE is provided in Section 6.1. The accuracies of the regression models are compared in Section 6.2, while in Section 6.3, the accuracy of the estimated ship motion is evaluated from various perspectives.

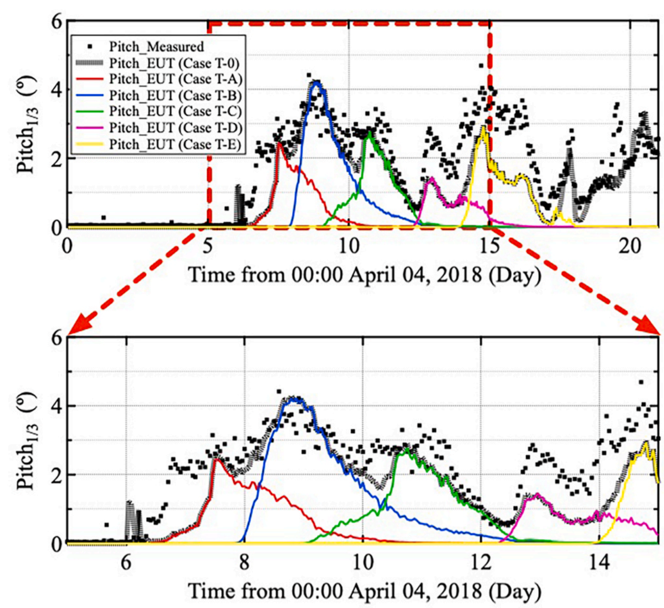

Fig. 26. Variations in ship motions separated by AD A – E for all wave frequencies.

6.1. Accuracy evaluation for each model

The accuracy of the different models was validated using standard metrics, including MBE and RMSE. The values for these standard metrics were obtained as follows:

$$MBE = \frac{1}{N} \times \sum_{i=1}^{N} (\hat{y}_i - y_i), \tag{15}$$

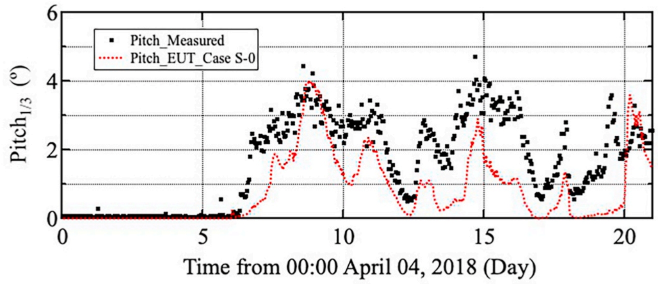

Fig. 27. Variations in ship motions for swell wave components.

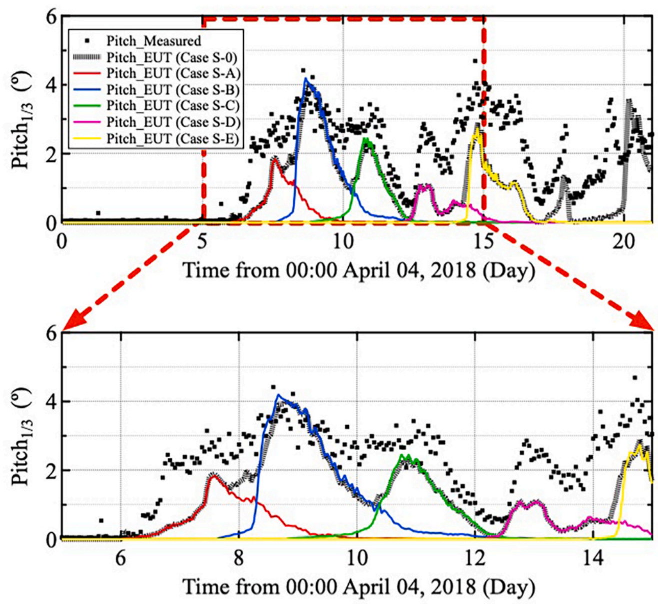

Fig. 28. Variations in ship motions separated by AD A–E for swell wave components.

$$RMSE = \sqrt{\frac{1}{N} \times \sum_{i=1}^{N} (\hat{y}_i - y_i)^2}, \tag{16}$$

where $\hat{y}_i$ is the predicted output, y_i is the measured value, and N is the number of measurements. Based on the values of *MBE*, we can evaluate each model for the degree of overestimation or underestimation using positive and negative signs, respectively. *RMSE* demonstrates the accuracy of the model by indicating how sensitive errors are in the results. Based on the values of *RMSE*, the accuracy could be compared regardless of positive or negative errors.

6.2. Evaluation of regression models for swell waves estimation

The regression models employed to estimate swell waves in Section 3 were evaluated, encompassing four regression models (Models I, II, III, and IV) and two data sources as inputs. This resulted in the comparison and evaluation of eight regression models. Fig. 29 illustrates the accuracy of several regression models assessed using MBE and RMSE.

As depicted in Fig. 29, the regression models utilizing the ERA5 reanalysis dataset displayed relatively small MBE and RMSE values. The lowest MBE value in both data sources was observed with Model III for the ERA5 reanalysis dataset (−0.2) and for the WW3 simulation results (0.1). The RMSE values with Model III exhibited a minimum value of approximately 0.53 with the ERA5 reanalysis dataset. However, Model IV displayed the most accurate with an RMSE value of 0.6 with the WW3 simulation results. Overall, it was established that the most accurate regression model was Model III using the ERA5 reanalysis dataset.

6.3. Evaluation of simulation results for ship motions using wave simulations

The estimated ship motions were evaluated in each case of wave simulation for all wave frequencies and simulations considering only swell wave frequencies. Additionally, wind inputs were defined for each atmospheric depression, A–E, as well as for all the depressions. Consequently, 12 cases were conducted to compare the reproduced accuracy with the ship motion. The estimated ship motions were compared and evaluated, as depicted in Fig. 30.

The values of MBE in pitch motion ranged approximately from −0.4 to −0.8, irrespective of the frequency or atmospheric depression conditions. Similarly, the values of RMSE in pitch motions hovered around 0.8 to 1.1, indicating similar accuracy in pitch motion across all cases. This suggests that the accuracy remained consistent for both total waves and swell waves. If the effect of swell waves were not significant, the ship pitch motion, considering only the swell waves, would have exhibited a larger difference. However, the results considering both total waves and only swell waves did not show a significant difference. It is evident that swell waves could be the primary influencing factors causing large ship motions.

Fig. 31 summarizes the flowchart of this study and its contributions. The characteristics of swell waves were analyzed using two methods: a regression model and a wave simulation model, and swell waves were reproduced for various cases. Despite some errors, the results for the estimated swell waves were deemed practically accurate. Further research in this area could contribute to the fields of port and shipping by proposing optimal ship routing strategies incorporating swell waves and developing a risk warning system for swell waves.

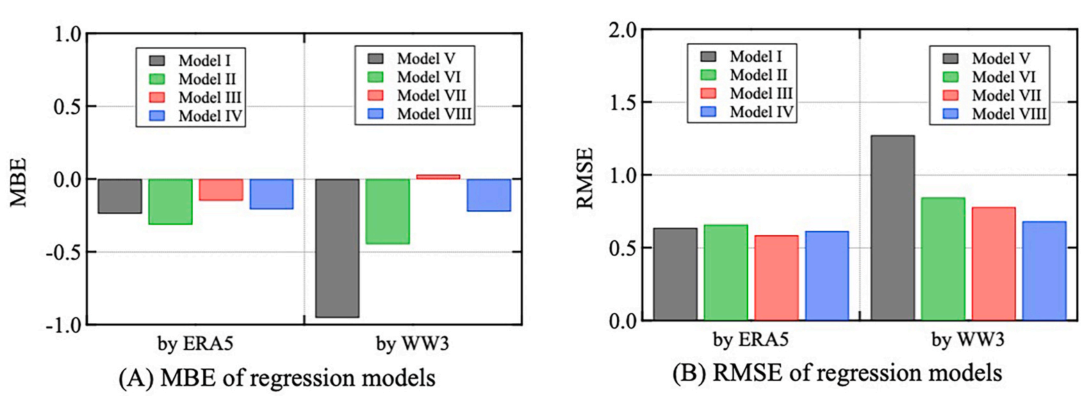

Fig. 29. MBE and RMSE of regression models for the estimated swell waves.

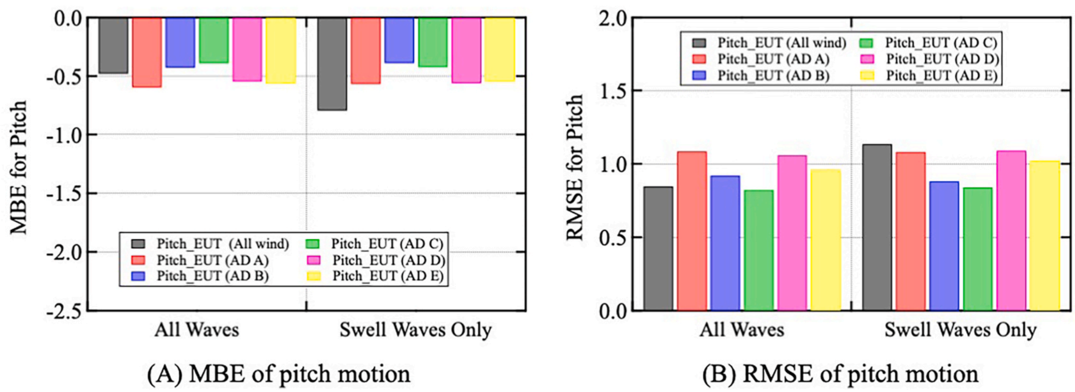

Fig. 30. MBE and RMSE of the estimated ship pitch motions.

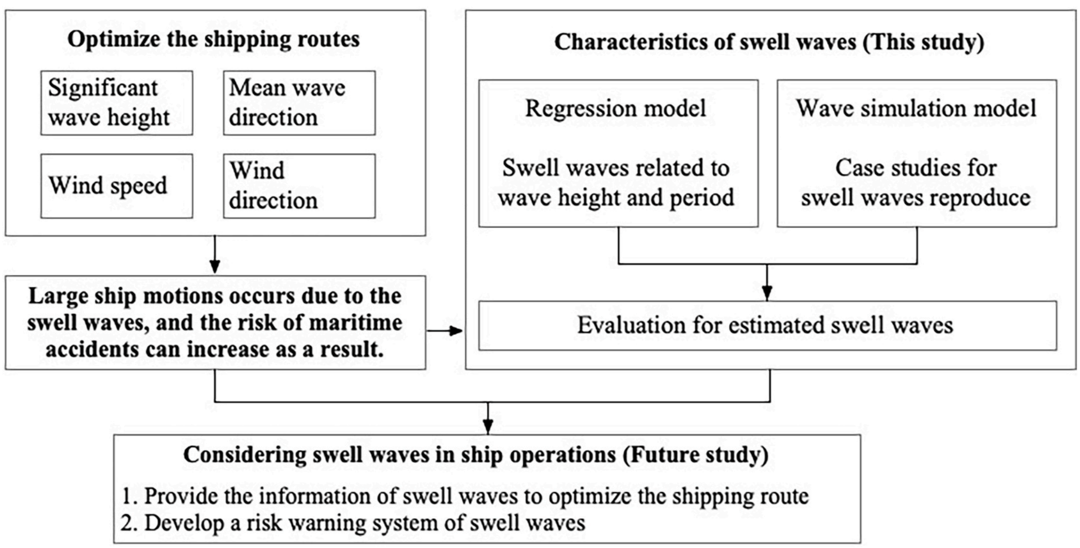

Fig. 31. Flowchart of contributions to the shipping industry.

7. Conclusions

Swell waves are known to significantly impact ships in the ocean or port facilities, yet their details remain elusive. In this study, we statistically analyzed these waves using ERA5 reanalysis data and onboard measured data for 63,000 DWT bulk carrier during voyages across the North Pacific Ocean in April 2018. Comparing the estimated swell waves from multiple regression models, regression model III, $\sqrt{H_{Total}} \times T_{mean}$ gives the most accurate estimation. This implies that a combination of wave height and period is important for estimating swell waves in the North Pacific Ocean.

Furthermore, wave simulations were conducted to numerically reproduce swell waves under various conditions. Although some differences with the ERA5 reanalysis data were observed in each case, the variation of swell waves could be practically reproduced as the summation of propagated swell waves from the generated wind waves in each atmospheric depression. This trend remained consistent even when the wave frequencies were limited to swell waves.

The results of the wave simulation were applied to estimate ship motions using the EUT model. The estimated ship motions were compared with measured ship motions to validate their accuracy and their influence on ships. It was observed that the estimated ship motions in all wave simulation cases were almost identical. Thus, the safety of ships is predominantly influenced by swell waves for ships exceeding 200 m in length across the North Pacific Ocean. Additionally, it was demonstrated that the estimation of swell waves and ship motions using the WW3 model and the EUT model can be practically accurate.

ERA5 has widely provided wave information, including swell waves. However, the original swell wave data from ERA5 showed inadequate results in areas where wind waves are dominant. This issue led to relatively low accuracy in the regression models using ERA5 data in this study. In contrast, the swell waves estimated by WW3 showed practically accurate results with the regression models. These issues should be carefully considered when using the original swell wave data from ERA5 in ship operations.

These findings can contribute to reducing economic and environmental losses in ship operations by providing characteristics of swell waves for optimal ship routing. Accurate information on swell waves can lead to more effective shipping routes with reduced fuel consumption and gas emissions. Furthermore, a risk warning system for swell waves can be developed to enhance the safety of ship and port operations in the future.

In this study, the properties of swell and wind waves were investigated for a specific sea area and season, namely, in the North Pacific Ocean in April 2018. Additionally, the analysis focused solely on Panamax-sized bulk carriers. Accumulating data on other situations in different sea areas, seasons, and ships is imperative in future studies, as shown in Fig. 31.

Funding

This study was financially supported by Scientific Research (B)

[Project number 20H02398, 2020–2024, represented by Kenji Sasa] and Fostering Joint International Research (B) [Project number 18KK0131, 2018–2022, represented by Kenji Sasa] under Grants-in-Aid for Scientific Research from the Japan Society for the Promotion of Science.

CRediT authorship contribution statement

Sang-Won Lee: Writing – original draft, Visualization, Validation, Software, Methodology, Data curation. **Kenji Sasa:** Writing – review & editing, Project administration, Methodology, Funding acquisition. **Tomoya Masagaki:** Visualization, Software, Formal analysis, Data curation. **Chen Chen:** Software, Methodology, Formal analysis, Data curation.

Declaration of competing interest

The authors declare that they have no known competing financial interests or personal relationships that could have appeared to influence the work reported in this paper.

Acknowledgments

The authors extend their gratitude to Shoei Kisen Kaisha, Ltd. And Imabari Shipbuilding Co., Ltd. For their cooperation in conducting on-board measurements of a 63,000 DWT bulk carrier from 2018 to 2019. We would like to thank Editage (www.editage.jp) for the English language editing.

Appendix 1. Simulated results for wave height separated by individual atmosphere depression

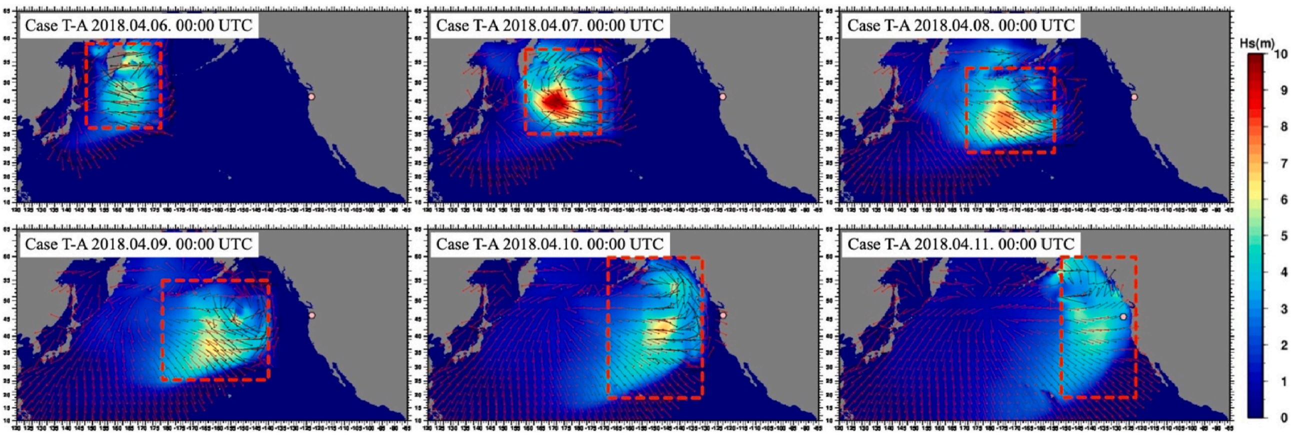

Fig. A.1. Distribution for simulated wave height separated by AD A (Case T-A).

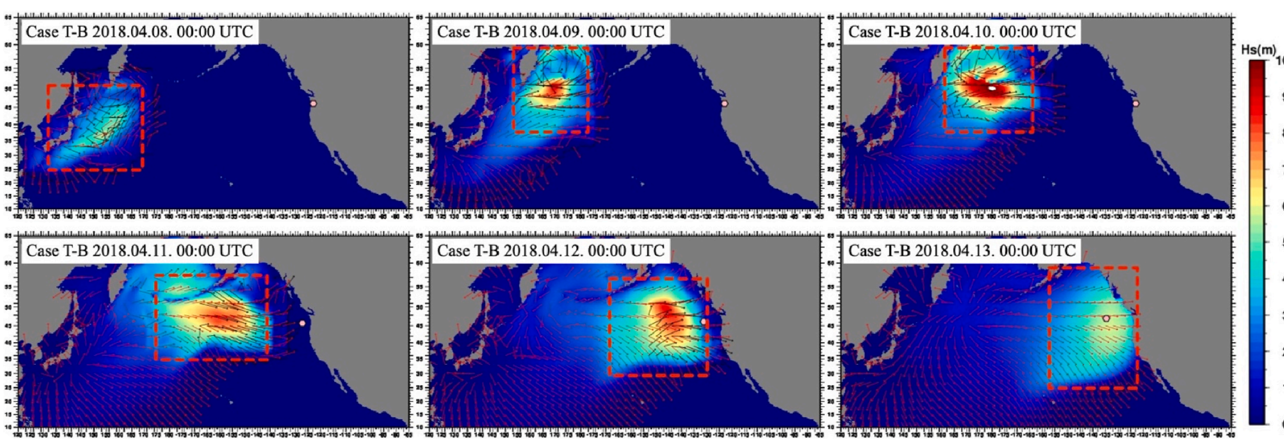

Fig. A.2. Distribution for simulated wave height separated by AD B (Case T-B).

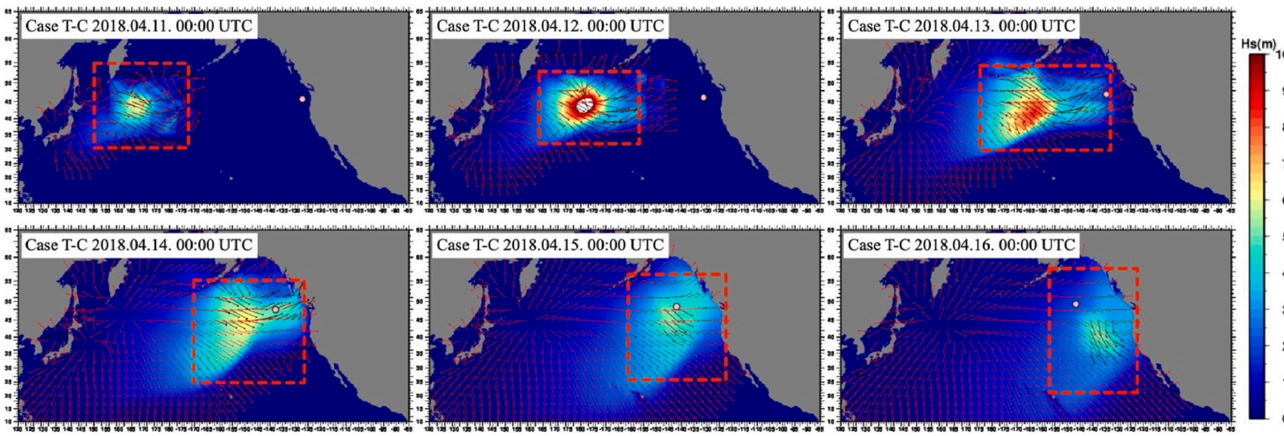

Fig. A.3. Distribution for simulated wave height separated by AD C (Case T-C).

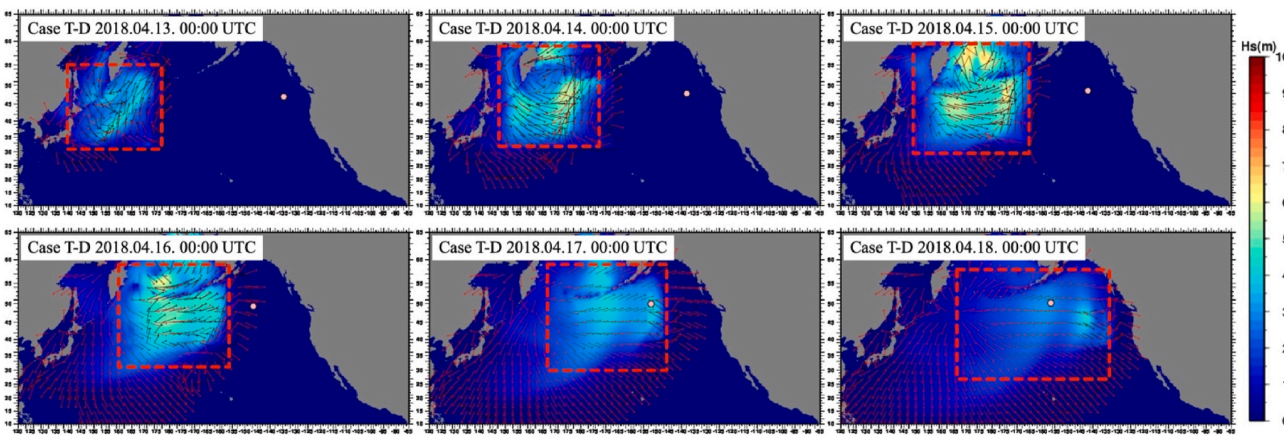

Fig. A.4. Distribution for simulated wave height separated by AD D (Case T-D).

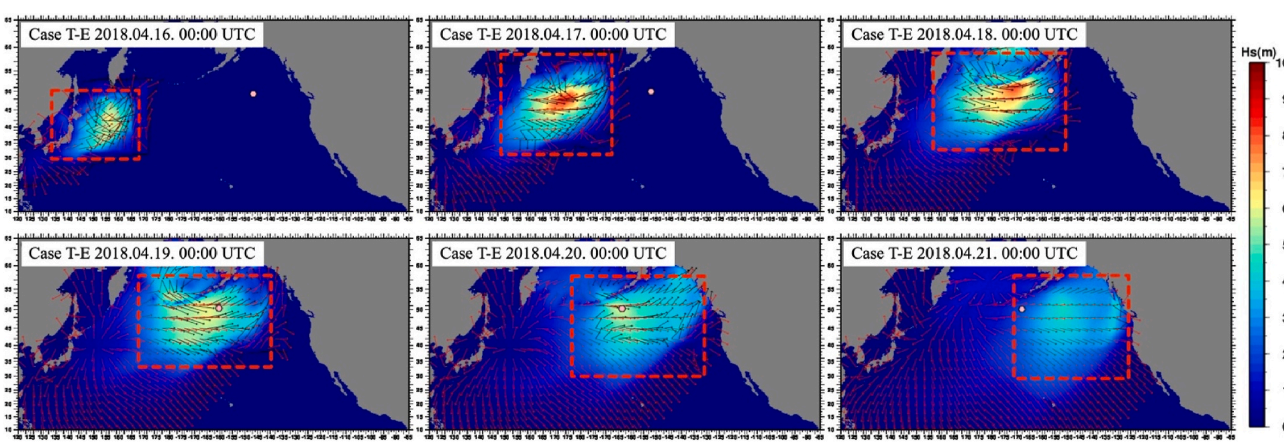

Fig. A.5. Distribution for simulated wave height separated by AD E (Case T-E).

Appendix 2. Simulated results for wave height separated by individual atmosphere depression for swell wave components

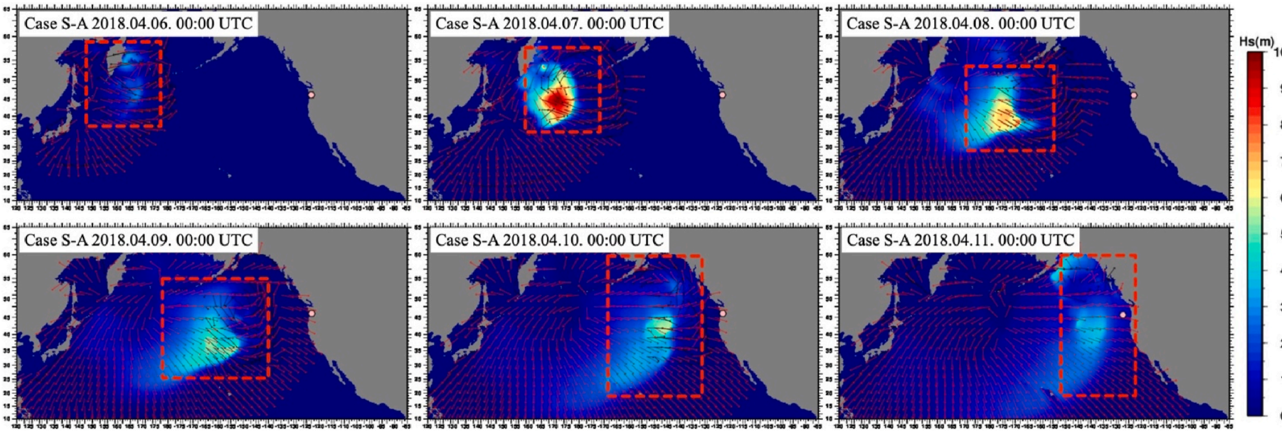

Fig. A.6. Distribution for simulated wave height separated by AD A for swell wave components (Case S-A).

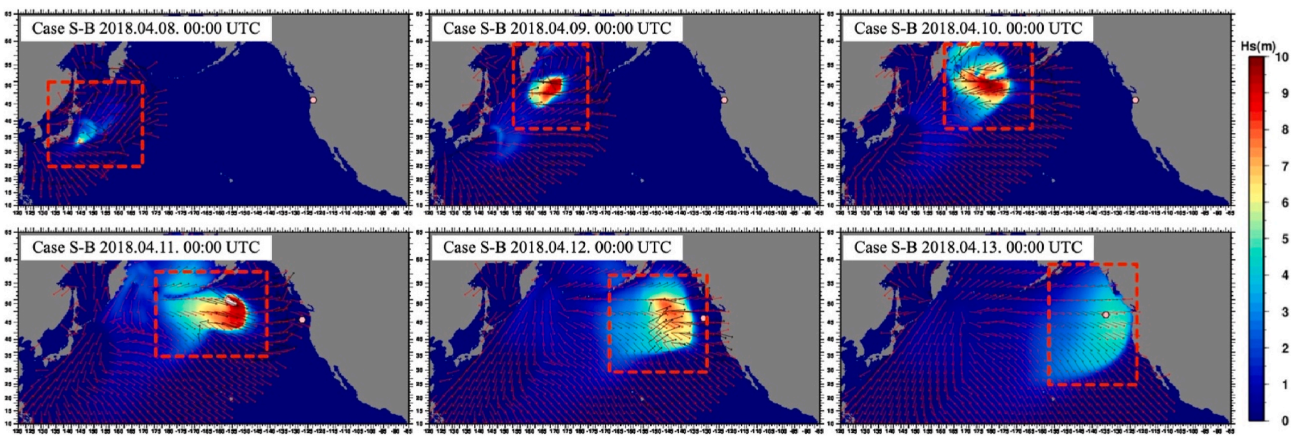

Fig. A.7. Distribution for simulated wave height separated by AD B for swell wave components (Case S-B).

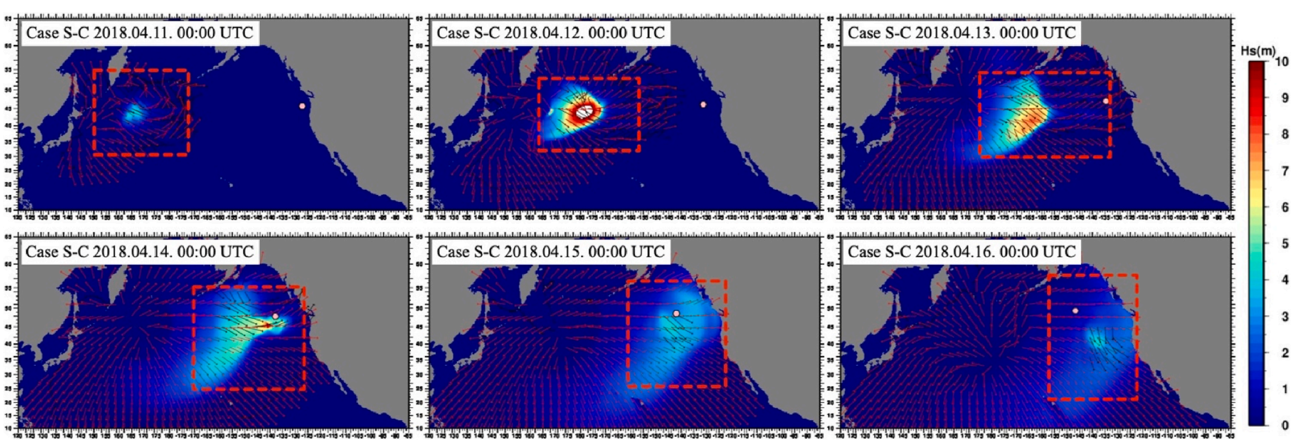

Fig. A.8. Distribution for simulated wave height separated by AD C for swell wave components (Case S-C).

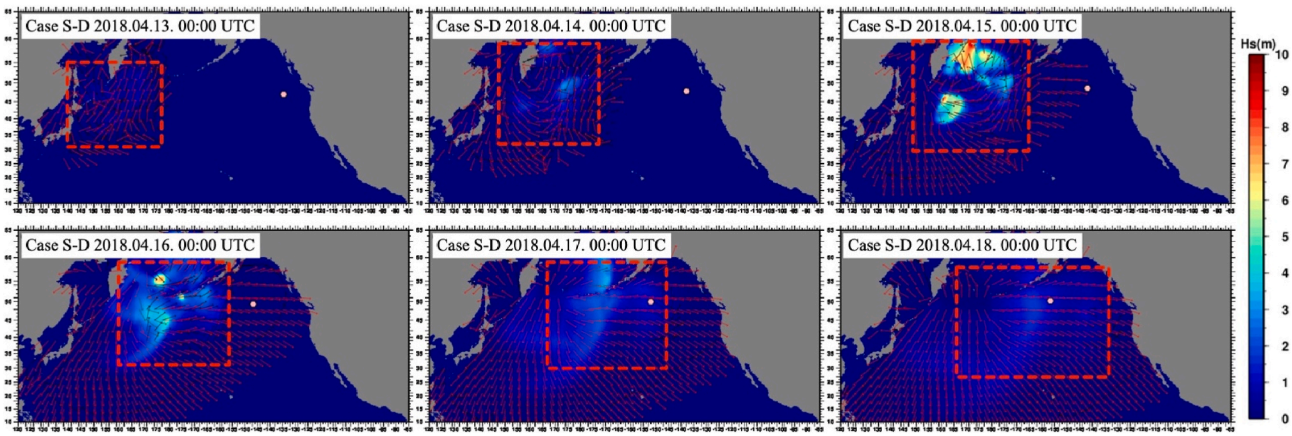

Fig. A.9. Distribution for simulated wave height separated by AD D for swell wave components (Case S-D).

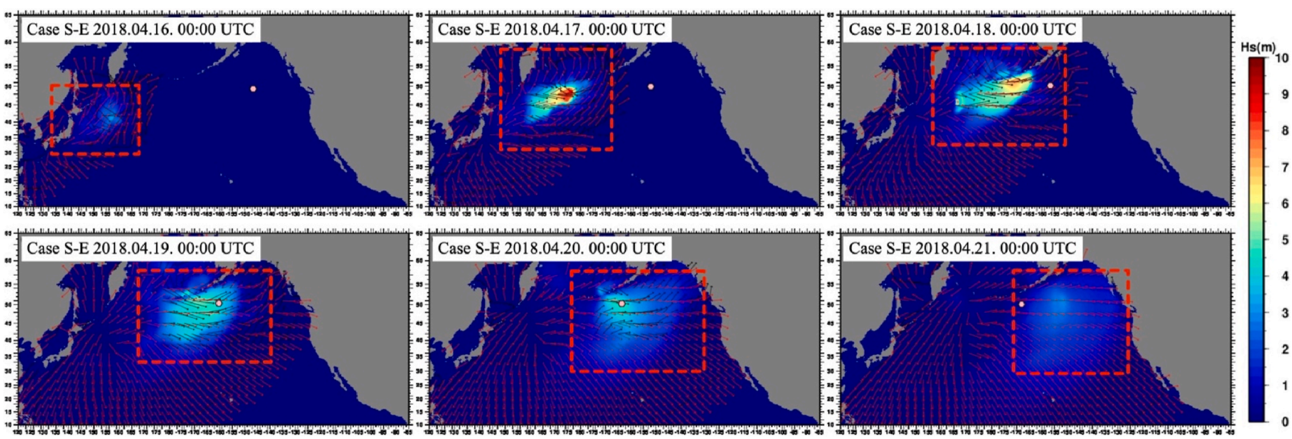

Fig. A.10. Distribution for simulated wave height separated by AD E for swell wave components (Case S-E).

References

Acanfora, M., Montewka, J., Hinz, T., Matusiak, J., 2017. Towards realistic estimation of ship excessive motions in heavy weather. A case study of a containership in the Pacific Ocean. Ocean Eng. 138, 140–150. https://doi.org/10.1016/j.oceaneng.2017.04.025.

Alves, J.H.G.M., 2006. Numerical modeling of ocean swell contributions to the global wind-wave climate. Ocean Model. 11, 98–122. https://doi.org/10.1016/j.ocemod.2004.11.007.

Alattabi, Z.R., Cahl, D., Voulgaris, G., 2019. Swell and wind wave inversion using a single very high frequency (VHF) radar. J. Atmos. Ocean. Technol. 36, 987–1013. https://doi.org/10.1175/JTECH-D-18-0166.1.

Booij, N., Holthuijsen, L.H., 1987. Propagation of ocean waves in discrete spectral wave models. J. Comput. Phys. 68, 307–326. https://doi.org/10.1016/0021-9991(87)90060-X.

Bruno, M.F., Molfetta, M.G., Totaro, V., Mossa, M., 2020. Performance assessment of ERA5 wave data in a swell dominated region. J. Mar. Sci. Eng. 8, 214. https://doi.org/10.3390/jmse8030214.

Carrasco, R., Horstmann, J., Seemann, J., 2017. Significant wave height measured by coherent X-band radar. IEEE Trans. Geosci. Rem. Sens. 55, 5355–5365. https://doi.org/10.1109/TGRS.2017.2706067.

Chen, C., Sasa, K., Ohsawa, T., Kashiwagi, M., Prpić-Oršić, J., Mizojiri, T., 2020. Comparative assessment of NCEP and ECMWF global datasets and numerical approaches on rough sea ship navigation based on numerical simulation and shipboard measurements. Appl. Ocean Res. 101, 102219 https://doi.org/10.1016/j.apor.2020.102219.

Chen, C., Sasa, K., Prpić-Oršić, J., Mizojiri, T., 2021. Statistical analysis of waves' effects on ship navigation using high-resolution numerical wave simulation and shipboard measurements. Ocean Eng. 229, 108757 https://doi.org/10.1016/j.oceaneng.2021.108757.

Costas, R., Figuero, A., Sande, J., Pena, E., Guerra, A., 2022. The influence of infragravity waves, wind, and basin resonance on vessel movements and related downtime at the Outer Port of Punta Langosteira, Spain. Appl. Ocean Res. 129, 103370 https://doi.org/10.1016/j.apor.2022.103370.

Dee, D.P., Uppala, S.M., Simmons, A.J., Berrisford, P., Poli, P., Kobayashi, S., Andrae, U., Balmaseda, M.A., Balsamo, G., Bauer, P., Bechtold, P., Beljaars, A.C.M., van de Berg, L., Bidlot, J., Bormann, N., Delsol, C., Dragani, R., Fuentes, M., Geer, A.J., Haimberger, L., Healy, S.B., Hersbach, H., Holm, E.V., Isaksen, L., Kallberg, P., Kohler, M., Matricardi, M., McNally, A.P., Monge-Sanz, B.M., Morcrette, J.J., Park, B.K., Peubey, C., de Rosnay, P., Tavolato, C., Thepaut, J.N., Vitart, F., 2011. The ERA-Interim reanalysis: configuration and performance of the data assimilation system. Q. J. R. Meteorol. Soc. 137, 553–597. https://doi.org/10.1002/qj.828.

ECMWF (European Centre for Medium-Range Weather Forecasts), 2021. IFS documentation CY47r3 - Part VII: ECMWF wave model. https://www.ecmwf.int/node/20201.

Emergency Response Division, 2020. Office of response and restoration. National Ocean Service. Container Ship ONE Apus [Data Access]. https://incidentnews.noaa.gov/incident/10208.

Grifoll, M., Martorell, L., La Castells, M., Martinez de Oses, F.X., 2018. Ship weather routing using pathfinding algorithms: the case of Barcelona—Palma de Mallorca. Transport. Res. Procedia 33, 299–306. https://doi.org/10.1016/j.trpro.2018.10.106.

Hiraishi, T., Atsumi, Y., Kunita, A., Sekiguchi, S., Kawaguchi, T., 1997. Observation of long period wave and ship motion in Tomakomai port. In: Seventh Int. Offshore Polar Eng. Conf.. Honolulu, Hawaii, USA, May 1997.

Hirakawa, Y., Takayama, T., Hirayama, T., Susaki, H., 2016. Development of Mini-Buoy for short term measurement of ocean wave. OCEANS 2016 MTS/IEEE Monterey 1–4. https://doi.org/10.1109/OCEANS.2016.7761337. Monterey, CA, USA.

Honda, T., Hasumi, K., Ito, K., Oda, Y., 2013. Study on correlation between long-period waves and significant waves along Japanese coasts. J. Jpn. Soc. Civ. Eng. Ser. B3 (Ocean Eng.) 69, 640–645. https://doi.org/10.2208/jscejoe.69.I_640 (in Japanese).

Iseki, T., Baba, M., Hirayama, K., 2013. Hybrid bayesian wave estimation for actual merchant vessels. Mar. Navig. Saf. Sea Transp. Marit. Transp. Shipp. (TransNav2013) 293–298.

ITF (International Transport Forum), 2015. The impact of mega-ships. International Transport Forum Policy Papers, No. 10. OECD Publishing, Paris. https://doi.org/10.1787/5jlwvzcm3j9v-en.

Jiang, X., Xie, B., Bao, Y., Song, Z., 2023. Global 3-hourly wind-wave and swell data for wave climate and wave energy resource research from 1950 to 2100. Sci. Data 10, 225. https://doi.org/10.1038/s41597-023-02151-w.

Kalnay, E., Kanamitsu, M., Kistler, R., Collins, W., Deaven, D., Gandin, L., Iredell, M., Saha, S., White, G., Woollen, J., Zhu, Y., Chelliah, M., Ebisuzaki, W., Higgins, W., Janowiak, J., Mo, K.C., Ropelewski, C., Wang, J., Leetmaa, A., Reynolds, R., Jenne, R., Joseph, D., 1996. The NCEP/NCAR 40-year reanalysis project. Bull. Am. Meteorol. Soc. 77, 437–471. https://doi.org/10.1175/1520-0477(1996)077<0437:TNYRP>2.0.CO;2.
Kashiwagi, M., 1992. Added resistance, wave-induced steady sway force and yaw moment on an advancing ship. Ship Technol. Res. 39, 3–16.
Kashiwagi, M., 1997. Numerical seakeeping calculations based on the slender ship theory. Ship Technol. Res. 4, 167–192.
Kashiwagi, M., Sugimoto, K., Ueda, T., Yamasaki, K., Arihama, K., Kimura, K., Yamashita, R., Itoh, A., Mizokami, S., 2004. An analysis system for propulsive performance in waves. J. Kansai Soc. Nav. Archit. Jpn. 241, 1–16. https://doi.org/10.14856/jksna.2004.67 (in Japanese).
Lee, S.W., Sasa, K., Chen, C., Waskito, K.T., Cho, I.S., 2022. Novel safety evaluation technique for ships in offshore anchorage under rough seas conditions for optimal ship routing. Ocean Eng. 253, 111323 https://doi.org/10.1016/j.oceaneng.2022.111323.
Lee, S.W., Sasa, K., Aoki, S., Yamamoto, K., Chen, C., 2021. New evaluation of ship mooring with friction effects on mooring rope and cost-benefit estimation to improve port safety. Int. J. Nav. Archit. Ocean Eng. 13, 306–320. https://doi.org/10.1016/j.ijnaoe.2021.04.002.
Lopez, M., Iglesias, G., 2014. Long wave effects on a vessel at berth. Appl. Ocean Res. 47, 63–72. https://doi.org/10.1016/j.apor.2014.03.008.
Lu, L.F., Sasa, K., Sasaki, W., Terada, D., Kano, T., Mizojiri, T., 2017. Rough wave simulation and validation using onboard ship motion data in the southern hemisphere to enhance ship weather routing. Ocean Eng. 144, 61–77. https://doi.org/10.1016/j.oceaneng.2017.08.037.
Ludeno, G., Serafino, F., 2019. Estimation of the significant wave height from marine radar images without external reference. J. Mar. Sci. Eng. 7, 432. https://doi.org/10.3390/jmse7120432.
Nielsen, U.D., 2007. Response-based estimation of sea state parameters — influence of filtering. Ocean Eng. 34, 1797–1810. https://doi.org/10.1016/j.oceaneng.2007.03.002.
Nielsen, U.D., 2008. The wave buoy analogy — estimating high-frequency wave excitations. Appl. Ocean Res. 30, 100–106. https://doi.org/10.1016/j.apor.2008.07.002.
Notteboom, T., 2020. Academic perspectives on the feasibility of mega container ships. Port Technology International 103 [Data Access]. https://www.porteconomics.eu/academic-perspectives-on-the-feasibility-ofmega-container-ships/.
Papadionysiou, S., 2014. Analysis of the Economics of Valemax Vessels. Norwegian School of Economics. Master thesis. http://hdl.handle.net/11250/275766.
Phillips, O.M., Banner, M.L., 1974. Wave breaking in the presence of wind drift and swell. J. Fluid Mech. 66, 625–640. https://doi.org/10.1017/S0022112074000413.
Portilla, J., Ocampo-Torres, F.J., Monbaliu, J., 2009. Spectral partitioning and identification of wind sea and swell. J. Atmos. Ocean. Technol. 26, 107–122. https://doi.org/10.1175/2008JTECHO609.1.
Safety4sea, 2012. Giant ValeMax ship completes maiden journey to China. https://safety4sea.com/giant-valemax-ship-completes-maiden-journey-to-china/. (Accessed 30 April 2024).
Sakakibara, S., Kubo, M., 2008. Characteristics of low-frequency motions of ships moored inside ports and harbors on the basis of field observations. Mar. Struct. 21, 196–223. https://doi.org/10.1016/j.marstruc.2007.11.002.
Sasa, K., 2017. Optimal routing of short-distance ferry from the evaluation of mooring criteria. Proc. Int. Conf. Offshore Mech. Arct. Eng. 6, 1–8. https://doi.org/10.1115/OMAE2017-61077.
Sasa, K., Chen, C., Fujimatsu, T., Shoji, R., Maki, A., 2021. Speed loss analysis and rough wave avoidance algorithms for optimal ship routing simulation of 28,000-DWT bulk carrier. Ocean Eng. 228, 108800 https://doi.org/10.1016/j.oceaneng.2021.108800.
Sasa, K., Lee, S.W., Shimada, R., Takagaki, T., Terada, D., 2023. Safety evaluation of lashed trailer motions in ferry operations under rough sea conditions. Ocean Eng. 275, 114114 https://doi.org/10.1016/j.oceaneng.2023.114114.
Suganuma, H., Kamiya, M., Atumi, Y., Koizumi, N., 1995. Examination of the frequency of occurrence of long-period waves and prediction of ship vibration occurrence through on-site observation. J. Jpn. Soc. Civ. Eng. Ser. B2 (Coast. Eng.) 42, 951–955. https://doi.org/10.2208/proce1989.42.951 (in Japanese).
Takashima, K., Mezaoui, B., Shoji, R., 2009. On the fuel saving operation for coastal merchant ships using weather routing. In: The International Journal on Marine Navigation and Safety of Sea Transportation. CRC Press, pp. 401–406.
Terada, D., Kosao, M., Oda, H., Sasa, K., Tanaka, Y., 2021. Estimation of characteristics of waves encountered with a ship by using a set of data obtained from draft measurement system. J. Jpn. Inst. Navig. 145, 47–55. https://doi.org/10.9749/jin.145.47 (in Japanese).
Tolman, H.L., 1989. The numerical model WAVEWATCH: a third-generation model for hindcasting of wind waves on tides in shelf seas. Faculty of Civil Engineering, Delft University of Technology. ISSN 0169-6548.
Tolman, H.L., 2014. User manual and system documentation of WAVEWATCH III Version 4.18. Natl. Ocean. Atmos. Admin./Natl. Weather Serv./Natl. Cent. Environ. Predict. (NOAA/NWS/NCEP) 282. Technical Note.
UNCTAD (United Nations Conference on Trade and Development), 2023. Review of Maritime Transport, p. 157. https://doi.org/10.18356/9789213584569. New York; Geneva.
Villefer, A., Benoit, M., Violeau, D., Teles, M., 2023. Spectral wave modeling of bimodal sea states at laboratory and coastal scales. Ocean Model. 183, 102182 https://doi.org/10.1016/j.ocemod.2023.102182.
Vincent, C.L., Thomson, J., Graber, H.C., Collins III, C.O., 2019. Impact of swell on the wind-sea and resulting modulation of stress. Prog. Oceanogr. 178, 102164 https://doi.org/10.1016/j.pocean.2019.102164.
Waskito, K.T., Sasa, K., Chen, C., Kitagawa, Y., Lee, S.W., 2022. Comparative study of realistic ship motion simulation for optimal ship routing of a bulk carrier in rough seas. Ocean Eng. 260, 111731 https://doi.org/10.1016/j.oceaneng.2022.111731.
World Shipping Council, 2023. Containers lost at sea – 2023 update [Data Access]. https://www.worldshipping.org/statements/containers-lost-at-sea-2023-update.
Zhang, Z., Li, X., 2017. Global ship accidents and ocean swell-related sea states. Nat. Hazards Earth Syst. Sci. 17, 2041–2051. https://doi.org/10.5194/nhess-17-2041-2017.
Zheng, Z., Ma, X., Huang, X., Ma, Y., Dong, G., 2022. Wave forecasting within a port using WAVEWATCH III and artificial neural networks. Ocean Eng. 255, 111475 https://doi.org/10.1016/j.oceaneng.2022.111475.